Aerosol layer height (ALH) retrievals from oxygen absorption bands: Intercomparison and validation among different satellite platforms, GEMS, EPIC, and TROPOMI

Hyerim Kim[1,2], Xi Chen[1,2], Jun Wang[1,2,3], Zhendong Lu[2,3], Meng Zhou[4], Gregory R. Carmichael[1,2], Sang Seo Park[5], Jhoon Kim[6]

[1]Department of Chemical and Biochemical Engineering, The University of Iowa, Iowa City, 52242, USA
[2]Center for Global and Regional Environmental Research (CGRER), and Iowa Technology Institute, The University of Iowa, Iowa City, 52242, USA
[3]Interdisciplinary Graduate Program in Informatics, The University of Iowa, Iowa City, 52242, USA
[4]Goddard Earth Sciences Technology and Research (GESTAR) II, University of Maryland – Baltimore County, Baltimore, MD 21228, USA
[5]School of Urban and Environmental Engineering, Ulsan National Institute of Science and Technology (UNIST), Ulsan 689-798, Republic of Korea
[6]Department of Atmospheric Sciences, Yonsei University, Seoul 03722, South Korea

Correspondence to: Xi Chen (xi-chen-4@uiowa.edu); Jun Wang (jun-wang-1@uiowa.edu)

Abstract.

The vertical distribution of aerosols is crucial for assessing surface air quality and their impact on climate. Although aerosol vertical structures can be complex, assuming a certain shape for the aerosol vertical profile allows for the retrieval of a single parameter, the aerosol layer height (ALH), from passive remote sensing measurements. In this study, we evaluate ALH products retrieved using oxygen absorption measurements from multiple satellite platforms: the Geostationary Environment Monitoring Spectrometer (GEMS) focusing on Asia, the Earth Polychromatic Imaging Camera (EPIC) in deep space, and the polar-orbiting TROPOspheric Monitoring Instrument (TROPOMI). We use the extinction weighted aerosol optical centroid height (AOCH) derived from aerosol extinction profiles of Cloud-Aerosol Lidar with Orthogonal Polarization (CALIOP) as ground truth. The differences due to the inconsistent definitions of ALH in various retrieval algorithms are investigated and eliminated before comparison. We selected multiple dust and smoke cases under ideal observational conditions, referred to as "golden days," for the evaluation. Given the significant role of aerosol optical depth (AOD) in ALH retrieval, we first evaluated the AOD from these retrievals against the ground-based AErosol RObotic NETwork (AERONET). Results show that GEMS AOD at 440 nm has better agreement with AERONET AOD of ~0.9 correlation coefficient (R) than that at 680 nm, both of which underestimate with negative bias. In contrast, EPIC and TROPOMI tend to overestimate AOD by 0.33 and 0.23 for dust cases, respectively, while the bias for smoke plumes is small. Evaluation of ALH against CALIOP demonstrates that both EPIC and TROPOMI ALH have good consistency (R > 0.7) with CALIOP but overestimate by approximately 0.8 km. GEMS ALH displays minimal bias (0.1 km) but a slightly lower correlation (R = 0.64). Inter-comparisons among three passive retrievals indicate that GEMS retrievals have limited consistency with EPIC and TROPOMI of 0.3-0.4 R, while GEMS underestimate ALH of ~0.3 km and ~0.6 km compared with TROPOMI and EPIC, respectively. The correlations improve under conditions of higher absorbing aerosols (UVAI ≥ 3), as the signal in the oxygen absorption bands (O_2-O_2 used by GEMS) is enhanced. Although the ALH diurnal cycle from EPIC and GEMS shows some differences, they both demonstrate ALH descent in the afternoon, which might be related to the boundary layer process. Case studies show that EPIC ALH indicates a morning ascent to around 4.5 km, while GEMS ALH remains stable until declining to below 3 km in the afternoon.

1 Introduction

Atmospheric aerosols influence the Earth's energy budget and climate system by absorbing and scattering solar and terrestrial radiation (Wang and Christopher, 2003). The aerosol vertical distribution is one of the most important factors determining the aerosol radiative effects (Zhang et al., 2013). The altitude of absorbing aerosols such as dust and smoke affect the vertical distribution of radiative heating and modify the stability of the atmosphere (Babu et al., 2011; Koch and Del Genio, 2010; Wendisch et al., 2008; Wang and Christopher, 2006). When aerosols are lifted to high altitudes in upper troposphere and lower stratosphere, they can have longer residence times and transport over longer distance, influencing global radiative energy budget (Christian et al., 2019; Peterson et al., 2014). Aerosol vertical distribution influence the derivation of aerosol optical properties, such as aerosol optical depth (AOD) and single scattering albedo (SSA) in the ultra-violet (UV) spectrum where the top-of-atmosphere (TOA) radiance is also sensitive to the vertical variation of aerosols (Torres et al., 1998). Furthermore, estimates of surface concentration of particulate matter (PM) from the total columnar aerosol loading or AOD requires the knowledge or assumption about aerosol vertical distribution (Wang and Christopher, 2003). Aerosol profile is controlled by diverse processes, such as convective transport, in-cloud scavenging, particle growth by condensation, biomass burning emission and injection height, boundary layer mixing and more, depending on different sources and aerosol properties (Wang et al., 2006; Kipling et al., 2013; Yang et al., 2013; Kipling et al., 2016). Due to the complexity in these processes and lack of temporal and spatially resolved information, aerosol vertical profile has large uncertainty and diversity in chemical transport models (Wang et al., 2013; Yang et al., 2013; Koffi et al., 2016). Therefore, measuring accurate aerosol vertical distribution is still a challenge but critical in many research areas.

Satellite remote sensing techniques are effective for globally monitoring aerosol vertical profiles. Active satellite remote sensing, especially space-borne lidar such as Cloud-Aerosol Lidar with Orthogonal Polarization (CALIOP), on board with the Cloud-Aerosol Lidar and Infrared Pathfinder Satellite Observation (CALIPSO) platform, acquires backscatter profiles and retrieves aerosol extinction profiles with high vertical resolution (Winker et al., 2013). However, the global coverage of CALIOP is less than 0.2% due to its narrow swath and wide gaps between orbits. In contrast, the larger spatial coverage of passive remote sensing measurements overcomes this shortcoming. With the retirement of CALIPSO in August 2023, passive remote sensing will become the only routine technique accessible for the public at present from space for filling the data gap of measuring aerosol vertical distribution before next lidar dedicated to measure aerosols are launched into space. However, only limited information for aerosol extinction vertical profile can be obtained in passive remote sensing due to the need for multiple assumptions regarding surface and aerosol properties in the retrieval process (Geddes and Bösch, 2015; Rao et al., 2022). Several parameters, including spectral coverage, radiance, polarization, spectral resolution, signal-to-noise ratio (SNR), and the number of viewing angles, can influence the information content and retrieval uncertainties of aerosol profiles (Chen et al., 2021a).

Hence, many algorithms have been developed to extract a single piece of information regarding aerosol vertical distribution, with a primary emphasis on aerosol layer height, which approximates the altitude of aerosols of a presumed aerosol vertical profile. Passive sensing techniques to retrieve aerosol layer height (ALH) information include stereo photogrammetry, polarimetric techniques in UV-VIS spectrum, infrared (IR) technique, and atmospheric oxygen (O_2) absorption (Pierangelo et al., 2004; Muller et al., 2007; Zeng et al., 2008; Vandenbussche et al., 2013; Wu et al., 2016; Xu et al., 2018; Kim et al., 2023). Not only are these techniques based on different physical theories, but each product has

---

different definitions of ALH and parameterizations of aerosol profiles, including aerosol optical central height (AOCH),
150 aerosol effective height (AEH), etc. Part of this study will analyse how the assumption of the shape of aerosol vertical profiles in the retrieval may lead to inherent differences in the retrieval product. Beyond this theoretical analysis, this study mainly focuses on evaluating three ALH data products retrieved from three different satellite sensors that detect the TOA measurements in various O_2 absorption from visible to near-infrared bands.

155 Aerosols positioned at lower altitudes cause light to travel a longer path, resulting in increased absorption by O_2 molecules along the extended path (Ding et al., 2016; Xu et al., 2019). Consequently, the amount of scattered radiation received by satellites decreases as aerosol layer decreases in altitude. Kokhanovsky and Rozanov (2010) retrieved the top height of dust layer by fitting spectral TOA reflectance measurements from the O_2 A band (around 760 nm) of the Scanning Imaging Absorption spectroMeter for Atmospheric CHartographY (SCIAMACHY). Similarly, the official operational ALH
160 product of TROPOspheric Monitoring Instrument (TROPOMI) uses measurements of the O_2 A band to retrieve the centroid pressure or height of a presumed single aerosol layer (Nanda et al., 2020). However, retrieving ALH information over land, including areas with vegetation and soil surfaces, from the O_2 A band presents challenges. This is because the TOA reflectance in this band is dominated by high surface reflectance instead of aerosol scattering. Consequently, TOA reflectance becomes less sensitive to ALH, and errors in surface reflectance contribute to significant uncertainties in ALH
165 retrieval (Xu et al., 2019).

Despite the weaker oxygen absorption in the O_2 B band (near 688 nm) than in the O_2 A band, the surface reflectance is significantly lower in the O_2 B band across all land types, which proves advantageous for aerosol retrieval. Based on this principle, (Xu et al., 2017; Xu et al., 2019) have developed a retrieval algorithm that use measurements from both O_2 A
170 and B bands, applying it to observations from the Earth Polychromatic Imaging Camera (EPIC)/Deep Space Climate Observatory (DSCOVR) to produce a product known as aerosol optical central height (AOCH). Based on this algorithm, with several adjustments, an enhanced algorithm was developed and implemented in hyperspectral measurements from TROPOMI (Chen et al., 2021b) as TROPOMI AOCH. In comparison with the operational TROPOMI ALH product, which shows a bias of 2 km over land, TROPOMI AOCH shows a bias of approximately 0.5 km over both ocean and land (Chen
175 et al., 2021b; Nanda et al., 2020). Hence, in the context of this study, we employ TROPOMI AOCH retrieved through the combined utilization of the O_2 A and B bands, favoring it over the operational TROPOMI ALH product retrieved solely from the O_2 A band.

Furthermore, oxygen-dimer (O_2–O_2) absorption bands exhibit sensitivity to ALH similar to O_2 absorption bands. Aimed to
180 observe from 300 to 500 nm range, the Geostationary Environment Monitoring Spectrometer (GEMS) can measure radiation across multiple O_2–O_2 absorption bands, including 340, 360, 380 and 477 nm, with 477 nm found to be the most sensitive to the ALH due to its largest O_2–O_2 absorption (Chimot et al., 2017; Cho et al., 2024; Kim et al., 2020; Park et al., 2016). GEMS provides an aerosol layer height product, termed aerosol effective height (AEH), retrieved from the 477 nm O_2–O_2 absorption band. This algorithm has been applied in the Ozone Monitoring Instrument (OMI) measurements,
185 and recently been evaluated with CALIOP, revealing negligible bias and a standard deviation of 1.4 km in the AEH difference across the GEMS observation domain from January to June 2021 (Park et al., 2024; Park et al., 2016).

The three oxygen-related bands, namely, O_2–O_2 477 nm band, and the O_2 A and B bands, have differences in terms of oxygen absorption strength and surface reflectance, leading to their diverse sensitivities to ALH. Hence, comparing retrievals from different O_2 absorption bands can offer valuable insights into their respective advantages and limitations in ALH retrieval. This motivates us to validate three different satellite ALH products, GEMS, EPIC and TROPOMI, using CALIOP three-dimensional aerosol extinction product and conduct intercomparisons among them. While the validation of diurnal variations in ALH currently remains challenging, leveraging GEMS' hourly products alongside the near-hourly EPIC global retrievals allows us to conduct comparative analyses with the available data at hand.

Additionally, evaluation of ALH retrievals should consider the context of other retrieval parameters, such as AOD and UV aerosol index (UVAI). UVAI quantifies the difference between measured and calculated near-UV spectral dependence, with values near zero indicating an aerosol-free atmosphere or the presence of non-absorbing aerosols and clouds, while positive values are associated with UV-absorbing aerosols like carbonaceous aerosols, volcanic ash, and desert dust (Torres et al., 2007). Accurate retrieval of ALH requires reliable retrieval of AOD since the retrieval sensitivity is strongly dependent. Park et al. (2016) showed higher sensitivity of oxygen-dimer (O_4) slant column density to aerosol effective height at 477 nm with higher AOD. Xu et al. (2019) showed the sensitivity of Differential optical absorption spectroscopy (DOAS) ratios–the ratio of TOA reflectance between the absorption band and the continuum band–to ALH is enhanced for lower surface reflectance and higher AOD. Moreover, the sensitivity of UVAI to ALH, along with their correlation, rises with increasing AOD levels (Xu et al., 2019; Xu et al., 2017). Therefore, we evaluate AOD with Aerosol Robotic Network (AERONET), cross-compare AOD and UVAI products from different platforms as well as the relationship of ALH between products with different UVAI to see its impact.

Considering that the spatial coverage of CALIOP is limited, we carefully selected "golden" cases where dust and smoke events favor the retrievals from all three sensors. This selection can maximize the signal to noise ratio for ALH retrieval, and hence, the evaluation can shed light on the future improvement to bring the closure of various types of retrievals. Note that these conditions may differ from those observed on non-selected days. In addition to pixel-by-pixel comparison of these passive satellite products, they are also assessed with CALIOP aerosol extinction profiles along CALIOP's track. We provide a detailed comparison with CALIOP profiles for a dust and a smoke plume case. This paper outlines the data and comparison approach in section 2, followed by the comparison results for all data used in this study in section 3. Section 4 shows the investigation of the ALH variation during transport for selected dust and smoke cases. Lastly, conclusions and discussions are provided in section 5.

2 Data and methodology

The ALH products compared in this study share similarities in that they are all derived using oxygen (or its dimer) absorption bands and assume the same aerosol vertical profile shape. However, there are distinct variations in the specifics of each algorithm, including the definition of ALH, which may result in inherent differences in ALH retrievals. In section 2.1, we first introduce the characteristics of each passive product, providing some details of each retrieval algorithm, as well as presenting the retrieval performance from previous studies. The difference of ALH definitions is compared in section 2.2. Lastly, the approaches for comparing ALH data and evaluating them with ground-based observations or active measurements are illustrated in section 2.3.

2.1 Remote sensing data

2.1.1 GEMS / GK-2B

From a geostationary orbit about 36000 km above the equator, GEMS provides hourly measurements over Asia within the latitudes of 5˚S to 45˚N and the longitudes of 80˚E to 152˚E (Kim et al., 2020). Given the lower SNR in the morning due to large solar zenith angle (SZA), GEMS only scan the eastern half of the field of regard, leading to less products available over western region. The total amount of hourly products in each day also depends on the SZA in different seasons. The spatial resolution of GEMS products is 3.5×8 km (north-south and east-west) at Seoul, South Korea.

GEMS offers two products describing aerosol altitude, AEH and aerosol loading height, each derived from different algorithms. GEMS aerosol loading height, included in the level 2 GEMS aerosol product (L2AERAOD), employs an optimal estimation method, incorporating measurements at six wavelengths, including the O_2–O_2 band at 477 nm (Cho et al., 2024; Kim et al., 2018). In contrast, GEMS AEH algorithm uses the sensitivity of the O_2–O_2 band to the ALH similar to TROPOMI and EPIC using O_2 A and B bands, which will be discussed in the following subsection. Therefore, this study specifically focuses on analyzing GEMS AEH version 2.0.

GEMS AEH is retrieved using the O_2-O_2 slant column density (SCD) at 477 nm with a look-up table (LUT) approach adopting aerosol types, AOD, and SSA at 550 nm from L2AERAOD, and surface reflectance from the GEMS standard product for surface reflectance (Park et al., 2024). Three aerosol types were classified using UVAI and the Visible Aerosol Index (VisAI), which, similar to UVAI but with visible channels, categorizes aerosols into highly absorbing fine (HAF), dust, and non-absorbing (NA) aerosols. NA aerosols are selected when UVAI yields a negative value, the dust type is determined when both UVAI and VisAI are positive, and HAF is selected when UVAI is positive, but VisAI is negative (Cho et al., 2024). For LUT generation, aerosols are assumed to be spherical due to the computationally intensive spectral binning method, and the particle size distribution, refractive index, and fine mode fraction for each aerosol type are derived from the global AERONET inversion climatology (Cho et al., 2024).

Cho et al. (2024), validated GEMS AOD at 443 nm against AERONET data across the entire GEMS domain from November 1, 2021, to October 31, 2022. They found the total GEMS AOD showed a R value of 0.792, a root mean square error (RMSE) of 0.227, and a mean bias error (MBE) of 0.038. Park et al. (2024) retrieved and validated GEMS AEH with CALIOP AEH. The differences in AEH between GEMS and CALIOP for dust plume cases were -0.07 ± 1.09 and -0.11 ± 1.27 km, with 53.8% and 72.9% of all pixels showing differences less than 1.0 and 1.5 km, respectively. Moreover, during the period from January to June 2021, they observed an average AEH difference of -0.03 km.

2.1.2 EPIC / DSCOVR

Carried on the DSCOVR spacecraft at the Sun-Earth Lagrange-1 point (L1) 1.5 million km from the Earth, EPIC captures the image for sunlit disk of Earth every 60-100 mins per day. As a result, EPIC monitors the half globe near-hourly, rendering a full disk of 2048×2048 pixels at the spatial resolution of size of 12 km at the Earth surface (Marshak et al., 2018). With 10 narrow channels, EPIC detects the Earth-reflected solar radiance from ultraviolet, visible, to near-infrared (NIR) bands, including both O_2 A and B bands. Lower surface reflectance in O_2 B band compared to O_2 A band over land suggests that O_2 B band can be used to improve the ALH retrievals using O_2 A band only (Xu et al., 2019). Xu et al. (2017) developed an algorithm to retrieve aerosol optical central height (AOCH) from EPIC measurements in O_2 A and B bands at the first time and applied it for dust plumes in Atlantic Ocean. Later, Xu et al. (2019) added a smoke model in the LUT and applied it into several smoke plume cases over the Hudson Bay-Great Lakes area in North America.

Deleted: Satellite

Deleted: east

Deleted: west

Deleted: Aerosol Robotic Network (

Deleted:)

Deleted: close

Deleted: The fact that the lower

Deleted: than

Deleted: (Xu et al., 2019) motives us to use

Deleted: that use the

Deleted: solely.

280 They found that over 77 % collocated AOD pairs fell within an uncertainty envelope of ± (0.05 + 0.1 AOD), with a coefficient of determination (R^2) of 0.54. Based on this algorithm, Lu et al. (2021) updated the calibration of EPIC level 1 data and analysed the EPIC AOCH for U.S. smoke plumes during 2020 California big wildfires. The validation of EPIC AOCH against the extinction-weighted AOCH from lidar observations, CALIOP, in these papers show a high level of accuracy, with a correlation coefficient of 0.885 and a RMSE of 0.92 km for absorbing aerosols. The surface reflectance

285 data involves two sources: land surface reflectance is obtained from the MODIS surface bi-directional reflectance climatology, while water surface reflectance is derived from the GOME-2 surface Lambert-equivalent reflectivity (LER) database. Furthermore, a new LUT developed specifically for dust plumes in the East Asian region, based on multi-year AERONET inversion products, has been incorporated, as detailed in Lu et al. (2023).

290 **2.1.3 TROPOMI / S5P**

TROPOMI on board the Copernicus Sentinel-5 Precursor satellite was launched in October 2017 to measure solar radiation reflected by Earth from UV to shortwave infrared (SWIR) bands. This spectral range includes many trace gas absorption bands, and is also sensitive to aerosols and surface properties. Flying on a polar satellite, TROPOMI provides global atmospheric components products on a high spatial resolution, 5.5 km × 3.5 km (improved from 7 km × 3.5 km since

295 August 2019) once every day.

TROPOMI measures both O_2 A and B absorption bands, yet its official ALH product utilizes solely the O_2 A band measurements in its retrieval algorithm (Nanda et al., 2020). Chen et al. (2021b) developed an alternative algorithm suitable for TROPOMI data, enabling AOCH retrieval using both O_2 A and B bands. This approach draws upon the EPIC AOCH retrieval algorithm by Xu et al. (2019), employing the same LUT and least square method to optimize AOCH from the

300 ratio of O_2 absorption to its nearby continuum band. Enhancements include spectral resolution convolution into multiple narrow channels, a new cloud mask, and dust/smoke classification, with results reported in a standard latitude-longitude grid (0.05˚ × 0.05˚). Comparative analysis reveals that the AOCH exhibits approximately a 0.5 km bias over both ocean and land, contrasting with the 2 km bias observed in the operational ALH product from TROPOMI (Chen et al., 2021b; Nanda et al., 2020). Consequently, this study employs TROPOMI AOCH retrieval data, as previously highlighted in the

305 introduction. Furthermore, the new LUT developed for Asian dust plumes in EPIC retrievals has been integrated into the algorithm for application in East Asia. The surface reflectance data is the same used in the EPIC retrieval algorithm. The operational TROPOMI Level 2 UVAI product (Stein Zweers, 2022) is used to retrieve only pixels covered by absorbing aerosols with UVAI greater than 0.5.

310 **2.1.4 CALIOP / CALIPSO**

CALIOP is a lidar system on the CALIPSO platform that provides attenuated backscatter vertical profiles of aerosols and clouds in the atmosphere using a two-wavelength laser operating at 532 nm with linear polarization and at 1064 nm (Winker et al., 2009). While the global coverage of CALIOP is less than 0.2%, it provides high vertical resolution for retrieving aerosol extinction profiles (Winker et al., 2013). In this paper, we used CALIOP 5 km Level 2 aerosol extinction profile

315 product at 532 nm to derive optical depth weighted heights. Specifically, Level 2 Aerosol Profile, Version 4-21 data product for the year 2021 (CAL_LID_L2_05kmAPro-Standard-V4-21) is used. For the years 2022 to 2023, level 2 aerosol profile, version 4-51 (CAL_LID_L2_05kmAPro-Standard-V4-51) is used due to the data availability. To validate aerosol height

Formatted: English (UK)

Deleted: including

Deleted: gases

Deleted: the

Deleted: and aerosol information

Formatted: English (UK)

Deleted: look-up table (

Deleted:)

Deleted: level

Formatted: Font color: Text 1, English (UK)

325 retrievals from passive remote sensing with CALIOP observation, the optical depth weighted heights derived from CALIOP 5 km level 2 aerosol extinction profile product at 532 nm following previous studies are used (Chen et al., 2021b; Lu et al., 2023; Lu et al., 2021; Xu et al., 2019).

2.1.5 AERONET

330 AERONET is a ground-based remote sensing network to designed to measure and characterize aerosol optical properties through direct sun measurements taken with sun-sky scanning spectral radiometers (Holben et al., 1998). AERONET serves as a critical tool for validating satellite-retrieved aerosol optical properties including AOD. In this study, we used AOD data at 675 nm and 440 nm from AERONET Version 3 Level 1.5 to assess the accuracy of satellite AOD retrievals. AERONET sites located within our study domain of East Asia and Southeast Asia, as illustrated in Figure 2, were selected
335 for this analysis. Additional information of these sites can be found in Table S1.

2.2 Comparison of ALH Definitions

GEMS, TROPOMI, and EPIC algorithms all operate under the assumption that quasi-Gaussian vertical distribution of aerosol extinction described by parameters of loading, peak height (H), and half width (η) fixed at 1 km. The assumption
340 of a 1 km half width is grounded in typical Lidar observations for dust and smoke aerosols, as indicated by Reid et al. (2003). This value has also been used in the retrieval of AOD from UV observations by both the Total Ozone Mapping Spectrometer (TOMS) and OMI, as emphasized in the work by Torres et al. (1998). Presently, it is widely accepted as a standard parameter value, evident in products presented in this study. The aerosol extinction profile where z is the altitude with respect to surface can be expressed by a generalized distribution function as specified in Eq. (1):
345

$$\beta(z) = W \frac{\exp\left(-\sigma_H |z - H|\right)}{[1 + \exp\left(-\sigma_H |z - H|\right)]^2} \qquad \text{Eq. (1)}$$

where H is the altitude with peak aerosol extinction, W is normalization constant related to the columnar loading, and σ_H is the half width parameter defined as: $\sigma_H = \ln\left(3 + \sqrt{8}\right)/\eta$ (Spurr and Christi, 2014). However, ALH is a general term to describe the altitude of aerosol layer, while the definition of the retrieved ALH varies by algorithm. EPIC and TROPOMI
350 defined their retrieved ALH as H in Eq. (1) and referred to it as AOCH (Chen et al., 2021b; Lu et al., 2023; Lu et al., 2021; Xu et al., 2019; Xu et al., 2017). GEMS AEH is defined as the altitude above which the aerosol extinction is the $1/e$ of total columnar AOD, as described in Eq. (2):

$$\frac{\int_0^{AEH} \beta(z)dz}{\int_0^{TOA} \beta(z)dz} = 1 - e^{-1} \qquad \text{Eq. (2)}$$

355 In addition, AOCH retrieved from EPIC and TROPOMI O2AB-UI is relative to geographic (ground) surface, whereas GEMS AEH is relative to sea level. Henceforth, for simplicity and consistency, the term ALH will be used to refer to all aerosol height products used in this study, including GEMS AEH, TROPOMI AOCH, and EPIC AOCH. To validate

retrievals from passive remote sensing with lidar data, the optical depth weighted heights derived from CALIOP are used. We define CALIOP AOCH as the optical depth weighted height, as specified in Eq. (3):

Moved up [2]: 5 km level 2 aerosol extinction profile product at 532 nm following previous studies are used (Chen et al., 2021b; Lu et al., 2023; Lu et al., 2021; Xu et al., 2019).

$$AOCH_{CALIOP} = \frac{\sum_{i=1}^{n} \beta(z_i)\Delta z_i z_i}{\sum_{i=1}^{n} \beta(z_i)\Delta z_i} \qquad \text{Eq. (3)}$$

where $\beta_{ext,i}$ represents the 532 nm aerosol extinction coefficient at vertical level i with an altitude of z_i while Δz_i denotes the thickness of the vertical layer i.

The comparison of different definitions of ALH for the same aerosol vertical distribution is shown in Fig. 1. In an exampled aerosol extinction profile with EPIC or TROPOMI AOCH at 1.5 km, CALIOP AOCH stands higher at 1.65 km, with GEMS AEH being the highest at 1.87 km (Fig. 1a). The difference between EPIC/TROPOMI and CALIOP AOCH decreases as AOCH increases, ultimately disappears when CALIOP AOCH reaches approximately 4 km and above. When CALIOP AOCH is below ~1 km, EPIC/TROPOMI AOCH can be as large as 0.5 km lower than CALIOP. GEMS AEH exhibits a larger difference compared to CALIOP AOCH for higher AOCH, and this difference remains relatively constant at approximately 0.3 km for altitudes above ~3 km. Figure 1c illustrates that the difference between GEMS AEH and EPIC/TROPOMI AOCH can reach around 0.8 km near the surface. However, this difference decreases as AOCH increases, ultimately reaching 0.1 km for altitudes above ~3 km. In our further comparison of ALH, we count for these inherent differences by converting one definition to another to ensure consistency. Varying AOCH from 0-10 km, we created a LUT of AEH, EPIC/TROPOMI AOCH, and CALIOP AOCH corresponding to the same aerosol extinction profile according to their different definitions. Throughout this paper, we conducted two conversions to ensure consistency: first, we converted all passive sensor ALH products with the CALIOP AOCH definition for comparison with CALIOP data (Fig. 1b). Second, we converted GEMS AEH to the EPIC and TROPOMI AOCH definition for comparisons among passive remote sensing products (Fig 1c).
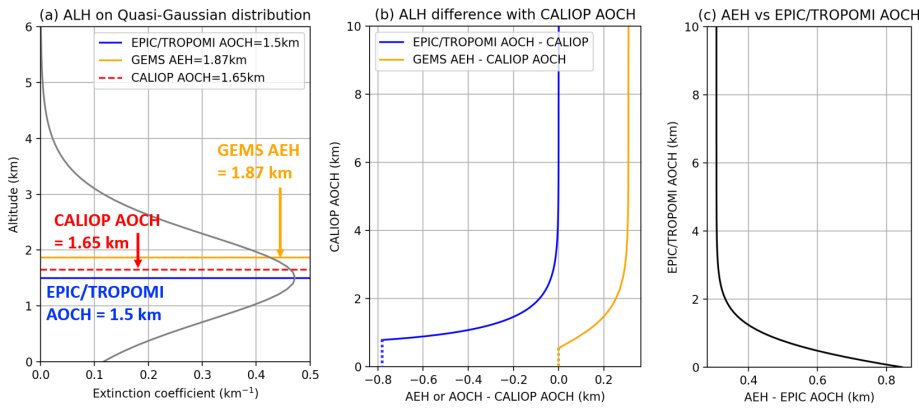
Figure 1. Comparison of ALH definition (GEMS, EPIC, TROPOMI, and CALIOP). (a) Relative heights within the quasi-Gaussian distribution when EPIC/TROPOMI AOCH is 1.5 km. (b) Difference between ALH from passive satellite with CALIOP

AOCH. Note that EPIC/TROPOMI AOCH is depicted as dotted vertical lines when it becomes negative below a specific CALIOP AOCH. (c) Difference between GEMS AEH and EPIC/TROPOMI AOCH definitions with respect to the altitude of EPIC/TROPOMI AOCH.

2.3 Comparison Approach

Given the availability of EPIC/TROPOMI retrievals for absorbing aerosols, we focus our comparison on a selection of "golden days" characterized by ideal viewing conditions for dust and smoke cases, excluding cloud-covered areas, as observed within GEMS field of regard from 2021 to 2023. These selected days are listed in Table 1 and correspond to the study domain depicted in Fig. 2. Classification of dust and smoke cases is determined by the predominant aerosol type identified in the CALIOP lidar data. Although EPIC products have similar temporal resolution to GEMS, observations over the research domain vary from 3 to 8 per day depending on the solar geometry. Flying on a polar orbit, TROPOMI only observed the whole globe once each day, but depending on the latitude of each case, TROPOMI ground track may overlap, which can lead to the possibility of two TROPOMI observations for some cases. Considering the differences in spatial and temporal resolutions among these three products, we first resample the GEMS product to TROPOMI and EPIC spatial resolution using the pixel area weighted method, and then linearly interpolate the GEMS product with time to match the observation time for the paired TROPOMI and EPIC data (Wang et al., 2020).
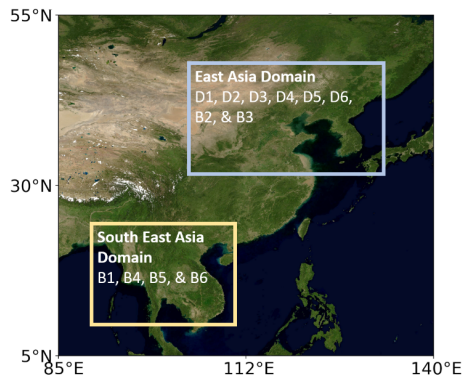
Figure 2. Study domains and cases. "D" represents dust cases, while "B" represents smoke cases ("B" for biomass burning). See Table 1 for more information. Map from Blue Marble: Next Generation from NASA Earth Observatory.

Table 1. Case study dates and the number of observations of each sensor for each domain.

Case no.	Date	Domain	Number of orbits (or granules)		
			GEMS	TROPOMI	EPIC
D1[a]	2021-03-28	East Asia	7	2	4
D2	2021-04-26	East Asia	8	2	7
D3	2022-04-10	East Asia	8	2	5
D4	2023-03-10	East Asia	7	2	3
D5	2023-05-19	East Asia	8	2	8

D6	2023-05-20	East Asia	8	2	7
B1	2021-03-31	Southeast Asia	6	1	5
B2	2021-08-10	East Asia	8	1	8
B3	2021-08-11	East Asia	6	2	8
B4	2022-04-09	Southeast Asia	8	2	5
B5	2023-03-26	Southeast Asia	6	1	5
B6	2023-04-17	Southeast Asia	8	1	4

ᵃ: The initial "D" means dust case and "B" represents smoke case from biomass burning.

415

UVAI data from GEMS, EPIC, and TROPOMI are also cross compared as UVAI is used in all retrieval algorithms. The ALH comparison and validation for different GEMS UVAI is conducted to analyze the possible distinction of GEMS AEH retrieval accuracy for different UVAI values. Furthermore, as the accuracy of each AOD product also influences corresponding ALH retrieval, AOD will be validated by the ground-based AERONET inversions. When matching satellite

420 pixels with ground sites, we consider the number of valid satellite retrievals within a 0.2º radius around AERONET sites. If the number of valid retrievals exceeds 30% of the total number of pixels, we compute the mean value of these retrievals and compare it with the corresponding AERONET AOD. The AERONET AOD is averaged for a period of 30 minutes before and after each satellite observation, aligning with the satellite overpass time (or observation time for GEMS). Furthermore, we only include satellite data points with a spatial standard deviation less than 0.3 to ensure spatial

425 consistency in the comparison. Since TROPOMI and EPIC AOD are retrieved at 680 nm, whereas GEMS AOD is retrieved at 443 nm, we estimate GEMS AOD at 680 nm from its AOD at 443 nm. This estimation is based on a combination of aerosol type (dust, HAF, NA) for each pixel and the Angstrom exponent (440 nm – 677 nm) from the GEMS aerosol model corresponding to the aerosol type (Kim et al., 2018). When co-locating passive satellite products with CALIOP pixels along the track, we employ a similar approach to the comparison with AERONET. This involves calculating the distance

430 from the center of the CALIPSO ground track within a range of 0.2º and adjusting the threshold for valid retrieval to exceed 30%.

3 Results

For all the dust and smoke cases listed in Table 1, the AOD products from GEMS, TROPOMI, and EPIC are first validated against the ground-based AERONET AOD data. Subsequently, a pixel-by-pixel intercomparison is conducted among the

435 satellite products. Additionally, the ALH products from the three passive satellite measurements undergo validation using CALIOP level 2 aerosol extinction profile. These validated ALH products are then intercompared.

3.1 AOD intercomparison and validation with AERONET

The validation of the AOD products from GEMS, TROPOMI, and EPIC against AERONET AOD is shown in Fig. 3. GEMS AOD at 443 nm exhibits a strong positive correlation with AERONET AOD at 440 nm, with correlation coefficients

440 (R) of 0.9 for dust cases and 0.88 for smoke cases (Fig. 3a). At 680 nm, the correlation for smoke cases remains high at R = 0.84, indicating a similar level of agreement with the 443 nm measurements. However, for dust cases at 680 nm, the correlation decreases to R = 0.73, along with a 17 % increase in RMSE, indicating distinct retrieval accuracy of GEMS AOD at 443 and 680 nm for dust. GEMS AOD at 680 nm show stronger underestimation than 443 nm, particularly

noticeable when AERONET AOD exceeds 0.5. Furthermore, the bias increases with higher AOD levels, as shown in Fig. S2. The observed underestimation of GEMS AOD at 680 nm can be in part due to an overestimation of the Angstrom Exponent (AE), which can be affected from inaccurate particle size or refractive index in the wavelength-dependent aerosol model.

For dust cases, both TROPOMI and EPIC AOD show a positive bias compared to AERONET AOD, with values of 0.23 and 0.33 for TROPOMI and EPIC, respectively. In contrast to the dust cases, TROPOMI and EPIC AOD exhibit a negligible bias and smaller RMSE for smoke cases. Although TROPOMI and EPIC AOD do not provide retrievals for values less than 0.2, many AERONET AOD data points exist with values under this threshold, particularly in dust cases. This suggests that the surface reflectance employed in the dust aerosol model from TROPOMI and EPIC may be underestimated, resulting in an overestimation in AOD retrieval. For TROPOMI and EPIC retrievals over land, climatological surface reflectance data from MODIS is employed. Additionally, unlike GEMS AEH retrieval algorithm that uses GEMS level 2 surface reflectance data, Cho et al. (2024) developed a new method for GEMS AOD retrieval, employing a novel hourly surface reflectance database generated through the minimum reflectance method, which integrates climatological minimum reflectance values for each pixel within a ±15-day window over a two-year period, along with monthly background AOD data. This novel surface reflectance estimation from GEMS AOD retrieval is shown effective. In summary, GEMS consistently underestimates AOD, especially at 680 nm, compared to AERONET AOD. EPIC and TROPOMI, while tending to overestimate AOD in dust cases due to underestimated surface reflectance, show a more accurate dust aerosol model than for smoke.

Deleted: S1

Formatted: Font color: Text 1

Deleted: Additionally, the comparison between EPIC and TROPOMI AOD with AERONET reveals a slope close to unity for dust cases (EPIC: 0.76, TROPOMI: 1.04), indicating the effectiveness of the dust aerosol model.

Deleted: Furthermore, the lower slope observed in the comparison for smoke cases (EPIC: 0.48, TROPOMI: 0.62) suggests that the smoke aerosol model is

Deleted: as accurate as the dust aerosol model. The positive y-intercept observed for both EPIC and TROPOMI
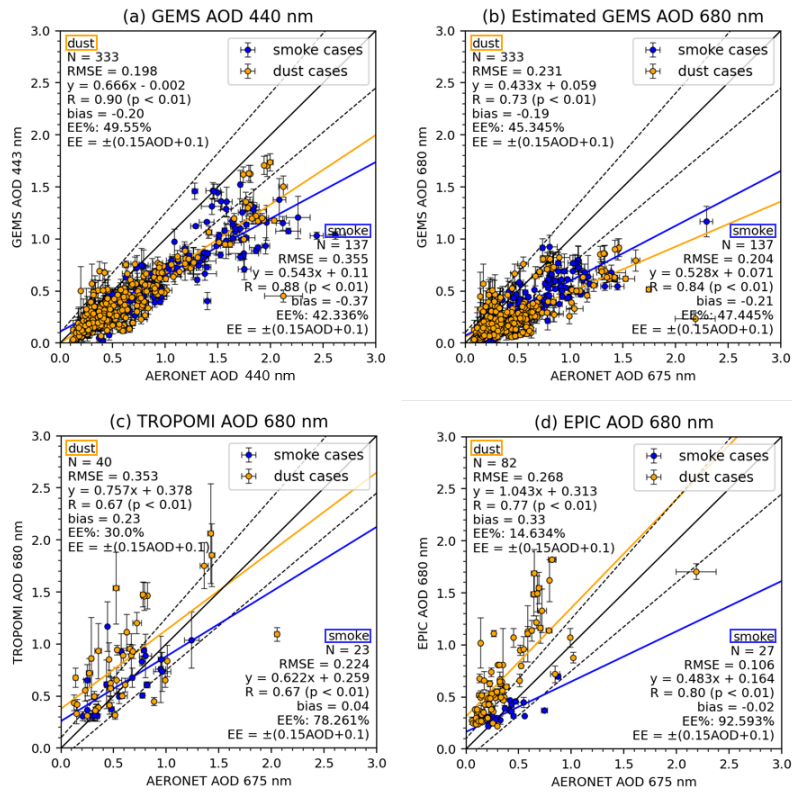
Figure 3. Comparison of GEMS, TROPOMI, and EPIC AOD with AERONET AOD for all cases. The blue and yellow dots denote smoke and dust cases, respectively. (a) Comparison of GEMS AOD at 443 nm with AERONET AOD at 440 nm. (b) Comparison of estimated GEMS AOD at 680 nm, (c) TROPOMI AOD at 680 nm, and (d) EPIC AOD at 680 nm with AERONET AOD at 675 nm. The solid black line is the 1:1 line, the solid lines are the regression lines, and the dotted lines are error envelops for AOD (EE = ± (0.15 AOD + 0.1)). Annotated are the number of scatter points (N), root mean square error (RMSE), correlation coefficient (R), significance level (p), mean bias, and the percentage of data points within the error envelop (EE). Satellite data points only with a standard deviation less than 0.3 are shown for spatial consistency.

Following the validation with AERONET AOD, Fig. 4 shows the comparison of GEMS AOD with TROPOMI and EPIC AOD, presented separately for dust and smoke cases. For dust cases, GEMS AOD is significantly lower compared with TROPOMI and EPIC, with negative mean biases of -0.44 and -0.53 for EPIC and TROPOMI, respectively. The inaccuracy of the GEMS dust aerosol model, as identified in the previous AERONET validation (Fig. 3), has a notable impact on the significant difference of GEMS AOD with TROPOMI and EPIC. Furthermore, surface reflectance issues observed in TROPOMI and EPIC further contribute to this disparity. Specifically, surface reflectance estimates for land surfaces from TROPOMI and EPIC may need refinement, as GEMS AOD values close to zero tend to be higher in TROPOMI and EPIC over land but not observed over water (Fig. S4). The smoke cases show a stronger agreement compared to dust cases, as indicated by decreased negative biases from -0.44 (-0.53) to -0.08 (-0.12) and RMSE values from 0.42 (0.45) to 0.24 (0.17)

Deleted: have

Deleted: S3

for TROPOMI (EPIC). The agreement is particularly robust between GEMS and EPIC, as indicated by a high R-value of
0.73. While the smoke aerosol model employed in TROPOMI and EPIC is not as effective as the dust model, its impact
510 on the comparison is relatively minor. These factors on the aerosol model including aerosol properties, fine mode fraction,
and the phase function, as well as the SSA, can largely influence the accuracy of AOD retrievals. Furthermore, AOD
sensitivity on changing SSA and surface reflectance is shown in Fig. S5. A detailed table including the aerosol models
employed in the AOD retrieval is provided in Table S6.

515
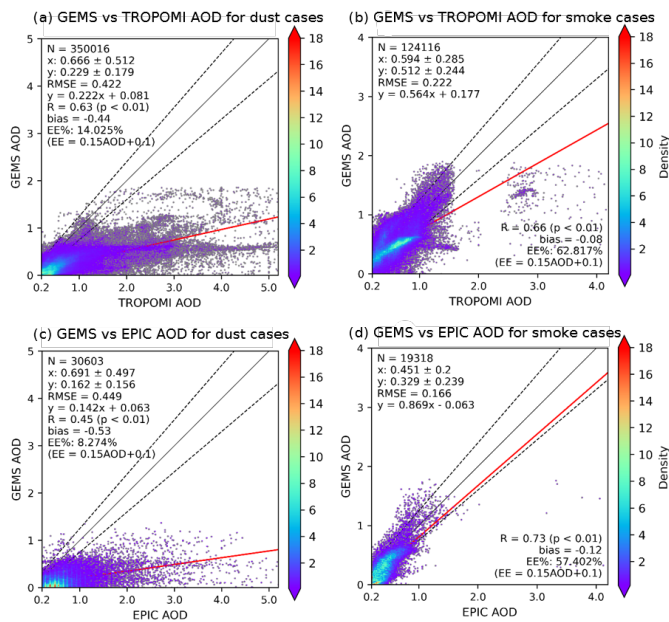
**Figure 4. GEMS AOD compared with the corresponding TROPOMI and EPIC products for dust and smoke cases. Scatter
density plots of (a) GEMS AOD versus TROPOMI AOD for dust cases, (b) same as (a) but for smoke cases, (c) GEMS AOD**
520 **versus EPIC AOD for dust cases, and (d) same as (c) but for smoke cases. Grey points indicate points where the data density is
less than 0.01. Black solid line is the one-to-one line, and the red solid line is the regression line. The dotted lines on the AOD
comparison plots (a), (c), indicates error envelops (EE = ± 0.15 AOD + 0.1). TROPOMI and EPIC AOD does not have retrieval
for less than 0.2, therefore, the figures axis start from where the data exists.**

525 **3.2 UVAI intercomparison**

The UVAI products of the three satellites are compared, since UVAI is used as a criterion to focus on retrieving absorbing
aerosols for the current TROPOMI and EPIC AOCH retrievals. Figure 5 compares GEMS UVAI with TROPOMI UVAI
(Fig. 5a) and EPIC UVAI (Fig. 5b) for all cases. Compared with TROPOMI, GEMS UVAI is systematically higher with
a positive mean difference of 1.21. Compared with EPIC, GEMS also exhibits a positive bias, although to a lesser extent
530 (0.32), and shows a higher correlation (R = 0.57). This suggests that when employing UVAI as a filtering criterion for
identifying absorbing aerosols in the EPIC and TROPOMI AOCH retrievals, it is important to establish a threshold that

takes into account the differences among these distinct products. The differences in the GEMS, TROPOMI, and EPIC

535 UVAI products can be caused by several reasons. First, different wavelengths are used to derive the UVAI product: GEMS UVAI is derived from radiances at 354 nm and 388 nm, whereas TROPOMI and EPIC UVAIs are derived from radiances at 340 nm and 380 nm. Additionally, pressure assumption and resolution differences can cause the differences of their UVAI retrievals. We included EPIC and TROPOMI UVAI comparison scatter plot in Fig. S7. To summarize, GEMS UVAI is systematically higher than TROPOMI and is more comparable to EPIC.

540
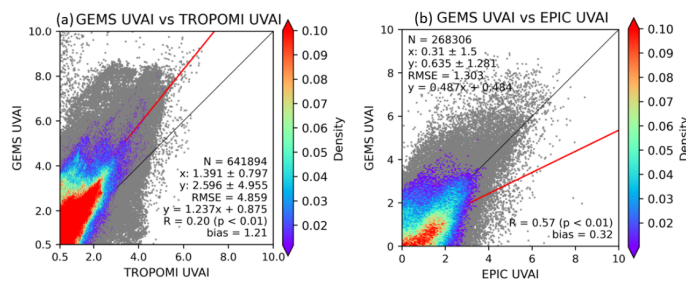
Figure 5. Comparison of GEMS UVAI with corresponding TROPOMI and EPIC products. Scatter density plots illustrating (a) GEMS UVAI vs. TROPOMI UVAI and (b) GEMS UVAI vs. EPIC UVAI. The one-to-one line is represented by a black solid line, while the regression line is shown in red. Grey points indicate points where the data density is less than 0.01. Dust and
545 **smoke cases are combined due to their similarity. Note that TROPOMI UVAI does not include retrieval values below 0.5, thus the axis begins at a minimum value of 0.5.**

3.3 ALH validation with CALIOP

To ensure the comparison of the same variable, it is critical to account for differences arising from different ALH definitions
550 as detailed in Section 2.2. As such, the ALH values of all passive sensors are converted to AOCH following the CALIOP AOCH definition when validated by CALIOP data. The comparison between the derived AOCH for the three passive sensors and the CALIOP AOCH is depicted in Fig. 6. Both EPIC and TROPOMI show higher AOCH values compared to CALIOP, with a bias of 0.8 km for both sensors. Additionally, the RMSE for EPIC and TROPOMI are 1.25 km and 1.31 km, respectively. In contrast, GEMS shows a minimal bias, accompanied by a lower RMSE of 0.75. Despite the
555 overestimation observed in EPIC and TROPOMI, their correlation with CALIOP is notably high (R=0.75 and R=0.71 respectively), while GEMS exhibits a slightly lower correlation (R=0.64). When valid data are available from all retrievals, the passive sensors show a notably high correlation with CALIOP AOCH (R > 0.9), with GEMS having the lowest RMSE (0.38 km), while EPIC and TROPOMI exhibit higher RMSE values of 1.54 km and 1.11 km, respectively (Fig. S8). Specifically, GEMS demonstrates the lowest RMSE (0.38 km), while EPIC and TROPOMI show larger RMSE values of
560 1.54 km and 1.11 km, respectively, with a tendency to overestimate ALH. The major contribution to the overestimations observed in EPIC and TROPOMI come from the smoke cases over Southeast Asia (B4, B5, and B6). This suggests a potential issue with the smoke aerosol model in the EPIC and TROPOMI AOCH algorithms when applied over Southeast Asia, which warrants further investigation. Furthermore, AOCH sensitivity on changing surface reflectance and SSA is shown in Fig. S4.

GEMS AEH algorithm retrieves both absorbing and non-absorbing aerosols, resulting in a larger dataset available for comparison. In contrast, EPIC and TROPOMI exclusively retrieve AOCH for absorbing aerosols, which are determined

570 based on UVAI (e.g., UVAI > 1 for TROPOMI and UVAI > 1.5 for EPIC). It is therefore desirable to assess the GEMS AEH retrieval accuracy under different aerosol characteristics. We categorize GEMS aerosol retrievals into two groups using a GEMS UVAI threshold of 3 (UVAI < 3 and UVAI ≥ 3) in the subsequent analyses (Fig. 6c-d). The overall agreement between GEMS and CALIOP is better for aerosols with UVAI ≥ 3 than those with UVAI < 3, particularly for dust cases, as evidenced by a higher R-value (0.75 compared to 0.42) and a lower RMSE (0.33 compared to 0.89). The

575 improved performance for UVAI ≥ 3 can be attributed to the stronger signals of aerosol layers detected in the O_2-O_2 absorption band. Furthermore, as observed in Fig. 6b, the mean bias of AOCH tends to be higher at 0.2 in smoke cases compared to -0.01 in dust cases.

580 **Table 2. Comparison of GEMS, TROPOMI, and EPIC AOCH with CALIOP AOCH measurements in Figure 6a.**

	N	EE (km)	RMSE (km)	Regression equation	x	y	R
GEMS	643	± 0.7	0.75	$y = 0.614\,x + 0.918$	2.1 ± 0.9	2.2 ± 0.9	0.64
EPIC	165	± 1.2	1.25	$y = 1.025\,x + 0.749$	2.5 ± 1.1	3.3 ± 1.4	0.75
TROPOMI	144	± 1.2	1.3	$y = 1.111\,x + 0.510$	2.4 ± 1.0	3.2 ± 1.5	0.71

Table 3. Comparison of GEMS with CALIOP AOCH for dust and smoke cases in Figure 6b-d.

	Dust cases					Smoke cases				
	N	R	RMSE (km)	Bias (km)	Regression equation	N	R	RMSE (km)	Bias (km)	Regression equation
All	267	0.46	0.771	0	$y = 0.684\,x + 0.63$	376	0.52	0.707	0.2	$y = 0.293\,x + 1.949$
UVAI < 3	193	0.42	0.884	-0.01	$y = 0.562\,x + 0.684$	308	0.55	0.656	0.34	$y = 0.315\,x + 1.931$
UVAI ≥ 3	74	0.75	0.328	0.03	$y = 0.636\,x + 0.511$	68	0.57	0.542	-0.46	$y = 0.468\,x + 1.239$

585
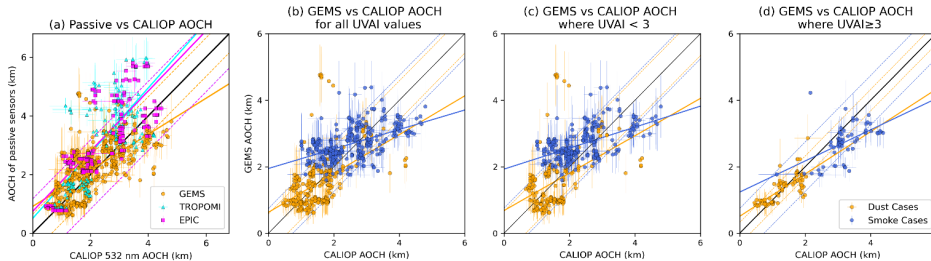
Figure 6. Comparison of GEMS, TROPOMI, and EPIC AOCH with CALIOP measurements for all cases. (a) Scatterplot of GEMS (orange), TROPOMI (cyan), and EPIC (magenta) AOCH versus CALIOP AOCH. The black solid line indicates one-to-one line and the dotted lines represent error envelop within which one standard deviation data points are for each passive satellite product. Panels (b) – (d) are scatter plots of GEMS versus CALIOP AOCH: (b) is for all data points, (c) is AOCH where GEMS UVAI < 3, and (d) is for AOCH where GEMS UVAI ≥ 3. For (b) – (d), orange dots indicate data points for dust cases and blue dots for smoke cases.

Based on a 2% measurement uncertainty for the EPIC DOAS ratios Geogdzhayev and Marshak (2018), the theoretical AOCH retrieval error is shown to remain below 1.25 km for vegetated surface when AOCH exceeds 1 km (Xu et al., 2019). Our analysis shows that the RMSE from all error sources, including measurement and retrieval uncertainties, evaluated between EPIC and CALIOP is approximately 1.25 km, which aligns with the retrieval error. The TROPOMI AOCH algorithm builds upon the framework established by the EPIC algorithm (Xu et al., 2019), with some adjustments for TROPOMI. Measurement uncertainty for TROPOMI is estimated to be 1 – 2 % (Kleipool et al., 2018). In addition to instrument errors, TROPOMI AOCH algorithm incorporates the convolution of TROPOMI spectral data, introducing potential additional uncertainty. Our study indicates an RMSE of 1.31 km for all error sources for TROPOMI AOCH. Assuming retrieval error similar to EPIC, this uncertainty appears reasonable. The GEMS AEH algorithm originates from Park et al. (2016), who performed an error analysis for OMI. The instrument error was indicated to be less than 10 m, stemming from a spectral wavelength error of 0.02 nm, with the total error ranging from 739 to 1276 m depending on aerosol types. Meanwhile GEMS has a spectral calibration accuracy of 0.002 nm (Kang et al., 2020). Our study demonstrates an RMSE of GEMS ALH at 0.75 km, falling within the theoretical retrieval error.

3.4 Passive ALH inter-comparison

Upon resampling GEMS products to match the spatial resolution of TROPOMI and EPIC, we synchronize the observation times through linear interpolation of the hourly GEMS products to facilitate a pixel-by-pixel comparison for all ALH products. To address the possible discrepancies stemming from different ALH definitions mentioned in Section 2.2, GEMS AEH is converted to align with the EPIC and TROPOMI AOCH definition. Furthermore, we categorize GEMS aerosol retrievals into two groups (UVAI < 3 and UVAI ≥ 3), similar to the analyses in Section 3.3.

The results of the ALH inter-comparison for both dust and smoke cases are given in Fig. 7. GEMS AOCH exhibits a narrower range compared to TROPOMI and EPIC, which can be attributed to the different range limits used in their algorithm LUT. GEMS only allows AEH to vary within the range from 0.2 to 5 km (Park et al., 2023), while EPIC and TROPOMI AOCH ranges from 0 to 9 km. Moreover, GEMS exhibits a negative mean difference of -0.25 and -0.62 when compared to EPIC and TROPOMI AOCH, observed across all dust and smoke cases, and across both UVAI classifications.

It is observed that aerosols with UVAI ≥ 3 exhibit a stronger correlation with GEMS AOCH compared with aerosols with UVAI < 3. This can be attributed to the O_2 or O_2-O_2 absorption band being more sensitive to aerosols with higher UVAI values. Setting the UVAI threshold to 4 enhances the statistical performance for UVAI ≥ 4, with an increase in correlation coefficients from 0.48 to 0.61 for TROPOMI and 0.39 to 0.46 for EPIC (Fig. S9).

625   Although our study cases show no CALIOP AOCH values above 5 km (Fig.6), TROPOMI and EPIC AOCH retrievals indicate values exceeding this altitude. This is a combination of inaccurate cloud detection and inherent sensitivity in the retrieval process of TROPOMI and EPIC. While some areas are influenced by cloud contamination, most of the high AOCH areas tend to have low AOD and not being influenced by clouds (Fig. S11 & S13). Since AOCH is more sensitive to higher AOD (Xu et al., 2017), there is greater uncertainty in AOCH retrievals in regions with lower AOD. Furthermore,

630   these high AOCH areas do not show high UVAI values greater than 4; instead, they exhibit values around 1-2, using GEMS UVAI as a reference. Therefore, both cloud detection inaccuracies and the low sensitivity of AOCH retrieval to low AOD contribute to the observed high AOCH in these areas, with the latter being more dominant in our selected cases.
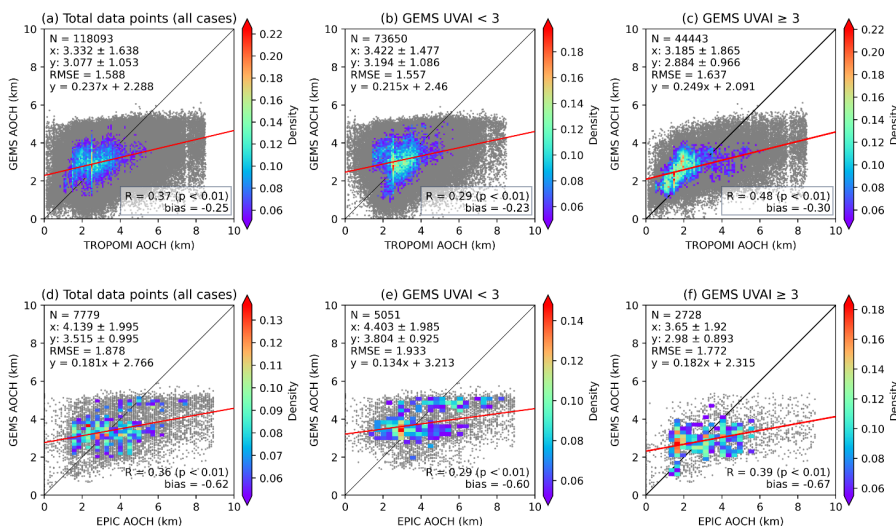
Figure 7. Intercomparison of AOCH values from GEMS, TROPOMI, and EPIC for all cases (dust and smoke combined) as a
635   function of UVAI. The density scatter plots show the AOCH comparison between GEMS and TROPOMI (a – c), and between GEMS and EPIC (d – f). (b) and (e) represent GEMS data for UVAI < 3, while (e) and (f) represent data for UVAI ≥ 3. GEMS AEH values have been converted to align with the AOCH definitions used by EPIC and TROPOMI.

3.5 Diurnal variation of GEMS and EPIC ALH

640   We present a comparison of the diurnal variations of ALH in GEMS hourly observations with near-hourly EPIC measurements, which provide between two to six daily observations within our region of interest. Our study domain encompasses a wide geographical area, with selected cases spanning from March to August, introducing seasonal changes that result in significant shifts in the sun's position. Therefore, we define the relative local solar noon time for a given day

Deleted: S6

Deleted: .

Deleted: S8 & S10

Deleted: AOCH

Deleted: cases

Deleted: Density

Deleted: plot of (a)

Deleted: AOCH comparison

Deleted: (d)

Deleted: AOCH comparison for all dust cases.

Deleted: c) are same as (a) but for

Deleted: , respectively. (e) and (f) are same as (d) but for GEMS UVAI < 3 and UVAI ≥ 3, respectively.

Deleted: into

Deleted: (or

Deleted:) AOCH definition

Deleted: close

as the moment when the solar zenith angle at a particular location reaches its minimum value. Using this relative local solar noon as a reference, we adjust the observation times of GEMS and EPIC products with relative local solar time (LST). Additionally, GEMS AEH was converted into the AOCH definition. Figure 8 illustrates the hourly diurnal variations of both GEMS and EPIC AOCH.

665   The diurnal pattern of EPIC AOCH values reveals a notable ascent in the morning, starting from heights below 3 km around 7-8 LST, peaking at approximately 4.5 km during 11-12 LST, followed by a marginal decline to approximately 3.5 km at 14-15 LST. Conversely, GEMS AOCH remains relatively stable (around 4 km) until a more pronounced descent occurs after 10 LST, reaching less than 3 km at 14-15 LST. Note that most of the time, GEMS AOCH values are lower compared to EPIC. The diurnal variation of AOCH reveals a slightly different pattern when UVAI exceeds 3 (Fig.
670   8b). GEMS AOCH when UVAI >3 shows a gradual increase until around 10-11 LST, followed by a notable decline, consistently maintaining lower AOCH values compared to the dataset inclusive of all UVAI values. Conversely, EPIC AOCH remains relatively steady until experiencing a rise between 10-14 LST, subsequently declining at 14-15 LST. There are notable differences in AOCH diurnal variation between GEMS and EPIC, with GEMS showing a significant decrease throughout the daytime, whereas EPIC exhibits a gradual increase followed by a subsequent drop.

675   Previous studies indicate that ALH tends to be higher in the afternoon, a phenomenon that may be partially affected by the PBLH. Xu et al. (2017) found higher EPIC AOCH in the afternoon, possibly indicating a relationship with the diurnal evolution of tropospheric convection. Lee et al. (2019) observed that aerosol heights tend to rise in the afternoon and early evening, likely due to the development of the boundary layer's mixed layer. Lu et al. (2023) conjecture that the diurnal cycle (rising in the morning and descending in the afternoon) of Saharan dust plume height is a consequence of the diurnal
680   variation in solar heating, which leads to thermal buoyancy lifting the dust layer, combined with the diurnal evolution of the boundary layer. Unfortunately, our dataset lacks sufficient information beyond 15 LST, making it challenging to discern the relationship between AOCH and PBLH, particularly when the PBL collapses in the late afternoon. Therefore, we examined three years of Modern-Era Retrospective Analysis for Research and Applications, Version 2 (MERRA-2) data from 2021 to 2023, focusing on March within the East Asia domain. MERRA-2 AOCH is defined same as the CALIOP
685   AOCH in the manuscript, weighted by optical depth at each vertical layer using aerosol extinction vertical profiles. A similar diurnal variation is observed between the PBLH and MERRA-2 AOCH calculated with the aerosol extinction below the PBLH (Fig. S10). This indicates that when most aerosols locate within the PBL, diurnal variation is affected by the PBL process, which changes the PBLH during daytime. The diurnal variation of EPIC AOCH from Fig. 8 is consistent with the MERRA-2 PBLH and AOCH calculated by extinction below the PBL, as ascending throughout the morning and
690   descending after 2 pm local time, although EPIC AOCH values are higher than MERRA-2 AOCH, due to its constraint by PBLH. The diurnal variation of GEMS and MERRA-2 AOCH show similarities for the afternoon decrease. However, GEMS AOCH, which shows an overall decrease throughout the day, does not coincide with the MERRA-2 data, which shows in increase until 14 local time. Despite the comparison of ALH diurnal variation from satellite observations and model reanalysis, the validation of the diurnal variation of ALH still remains a significant challenge due to a lack of
695   spatially and temporally resolved active remote sensing measurements. In addition, for passive remote sensing, potential artifacts such as scattering angle bias for geostationary satellites and contamination of cloud edges may influence the diurnal cycle of aerosol height. Additionally, the limited data points obtained from selected case study dates could introduce uncertainty when attempting to generalize the ALH diurnal cycle.
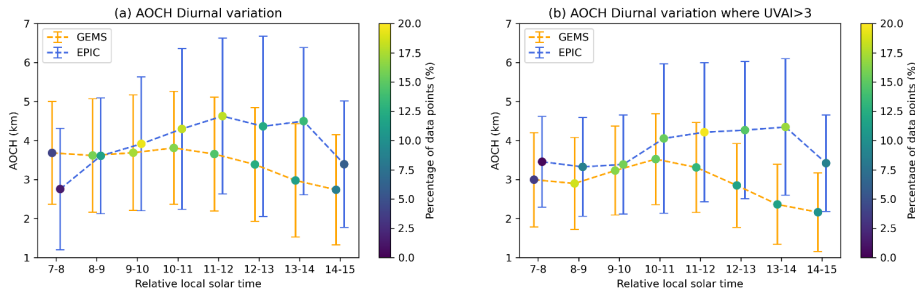
Figure 8. Diurnal variation of AOCH between GEMS and EPIC at relative local solar times. (a) AOCH diurnal variation for all pixels, (a) same as (a), but only for UVAI > 3. Yellow lines indicate GEMS AOCH error bar (standard deviation), blue indicates the corresponding of EPIC AOCH, dots represent the percentage of data points during each hour. GEMS AEH has been adjusted to match the EPIC AOCH definition.

4 Case study

We present detailed analysis of GEMS, EPIC, and TROPOMI ALH retrievals during transport for a dust (D1) and a smoke plume (B6). Diurnal variations of ALH from GEMS and EPIC for the dust or smoke cases are also discussed.

4.1 Dust plume case

Figure 9 shows GEMS, TROPOMI and EPIC ALH retrievals for a selected dust case on March 28, 2021 (D1). GEMS AEH was adjusted to EPIC/TROPOMI AOCH definition for consistent comparison. The first row presents GEMS AOCH, with magenta lines depicting CALIOP ground track over the GEMS map at the closest time of CALIOP measurement and the second row shows EPIC and TROPOMI AOCH aligned with the closest GEMS measurement time. The AOD, UVAI maps for all satellites are shown in the Fig. S11. This case is a spring dust event, originating from the Gobi Desert a few days before it reached over China on 28 March 2021, specifically near Beijing, indicated by the red star on the middle of the research domain (Fig. 9a). In the dust plume area, GEMS AOCH peaks at high values (~3 km) at 01:45 and 02:45 (Fig. 9a-b) before gradually decreasing to ~1.5 km by 06:45 (Fig. 9f). In contrast, EPIC and TROPOMI AOCH maintain a relatively consistent values at 1-2 km. For this dust case, hourly GEMS observations reveal clear hourly variations, while characterizing diurnal changes from TROPOMI and EPIC is challenging due to their limited number of observations compared to GEMS.

Deleted: S8	
Deleted: black	
Deleted: Likely	
Deleted: whereas discerning	
Deleted: is challenging with	
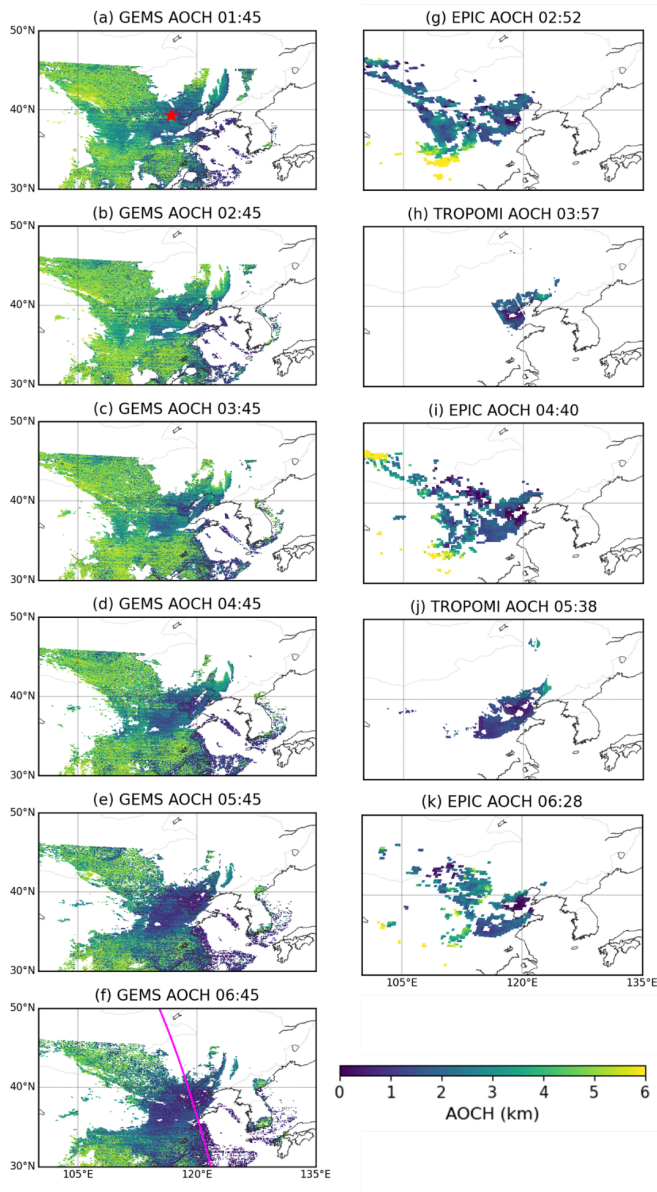
Figure 9. The first column (a – f) shows hourly GEMS AOCH (GEMS AEH adjusted to EPIC/TROPOMI AOCH definition) from (a) 01:45 to (f) 06:45 (UTC). Second column (g – k) EPIC and TROPOMI AOCH aligned with the nearest GEMS observation times for a dust plume event on 28 March 2021. The magenta line on the GEMS maps in the first column indicates the CALIOP ground tracks, which have the closest observation times with GEMS. The red star indicates the dust plume area near Beijing.

Deleted:
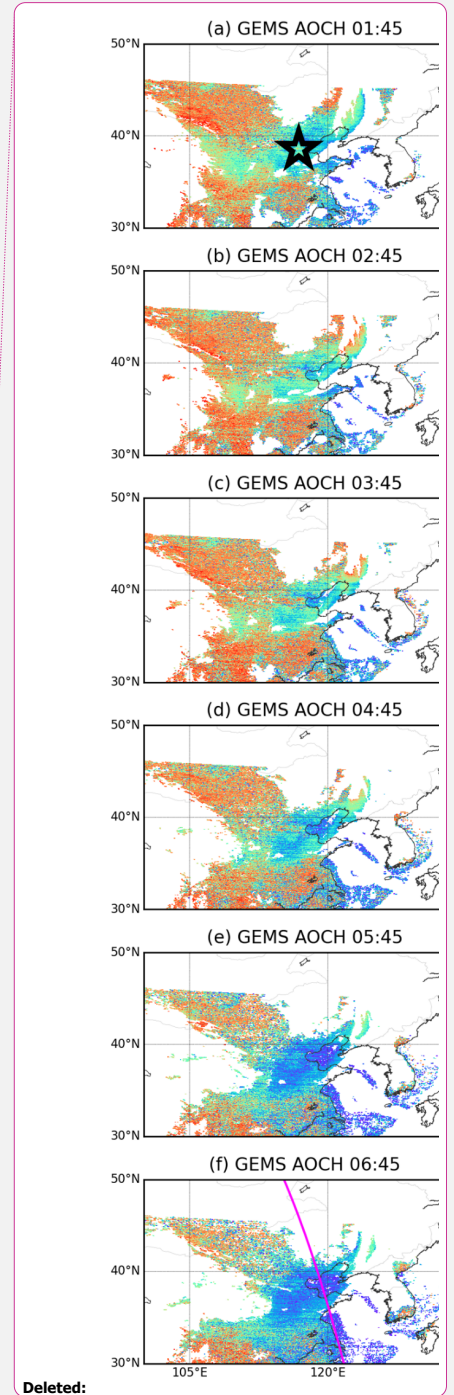
After converting all passive ALH products to the CALIOP AOCH definition, the comparison of GEMS, TROPOMI, and EPIC AOCH with CALIOP AOCH for this dust case was conducted and is shown in Fig. 10. GEMS has the greatest number of data points due to its valid retrievals for both scattering and absorbing aerosols and its high spatial resolution. For this specific case, EPIC AOCH show the highest correlation coefficient among all (R = 0.74) and TROPOMI AOCH also has a high correlation coefficient (R = 0.6) and the lowest RMSE of 0.33 km. Although CALIOP can capture multiple layers of aerosols from extinction coefficients, passive sensors used in this study assume single vertical profile, thereby retrieving AOCH where stronger signal is detected. In Fig. 10b, CALIOP identifies discontinuous high extinction coefficients at 38º N latitude and 119.5º E longitude leading to a discontinuous CALIOP AOCH. While EPIC AOCH shows the discontinuity from the absence of the retrieval in between the two layers, GEMS and TROPOMI exhibit continuous retrievals, consistently following the stronger signal. Consequently, discrepancies between CALIOP and passive sensors may be more pronounced in the presence of multiple aerosol layers. Further investigation is needed for a comprehensive study of multi-layered aerosol plumes.
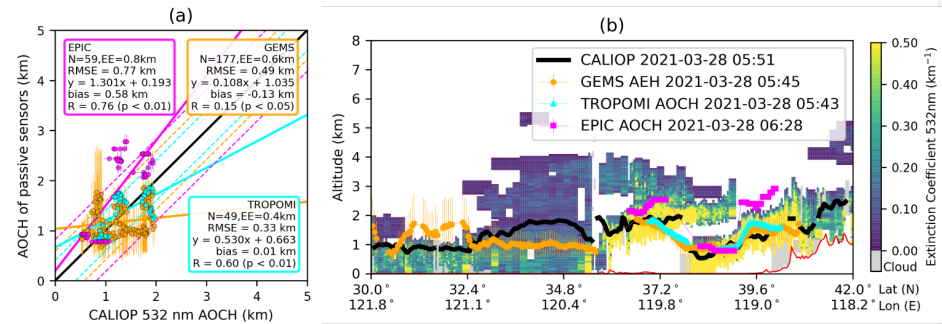
Figure 10. Comparison of GEMS, TROPOMI and EPIC AOCH with CALIOP AOCH for a dust case over East Asia on 28 March 2021. (a) GEMS, TROPOMI, and EPIC AOCH on the vertical profile of CALIOP aerosol extinction curtain plot. (b) Scatterplot of GEMS (orange), TROPOMI (cyan), and EPIC (magenta) versus CALIOP AOCH. All ALH products converted into the CALIOP AOCH definition.

Figure 11 shows the regional averaged ALH during this dust plume transport from 27 to 29 March 2021. To focus on the consistent area covered by the thickest dust plume, different UVAI thresholds were empirically selected. Pixels where UVAI values of their own products are higher than 3, 1, and 2 were considered for GEMS, TROPOMI, and EPIC, respectively. For CALIOP, collocated pixels along the track with GEMS UVAI > 3 were considered. Maps of regional ALH and UVAI for all products are provided in Fig. S11 and S12. The mean AOCH values of the dust plume from all products show good agreement, falling within reasonable error range of < 1 km. GEMS measurements show that the dust plume is located at 4-5 km on March 27, descends to ~3 km on March 28, and remains until March 29, consistent with EPIC and TROPOMI measurements. These daily changes in ALH reflects the atmospheric subsidence of dust aerosols during transport. Although daily mean of the AOCH values change during the plume transport, GEMS show similar diurnal variation each day, increase in early morning followed by a consistent decrease throughout the daytime.
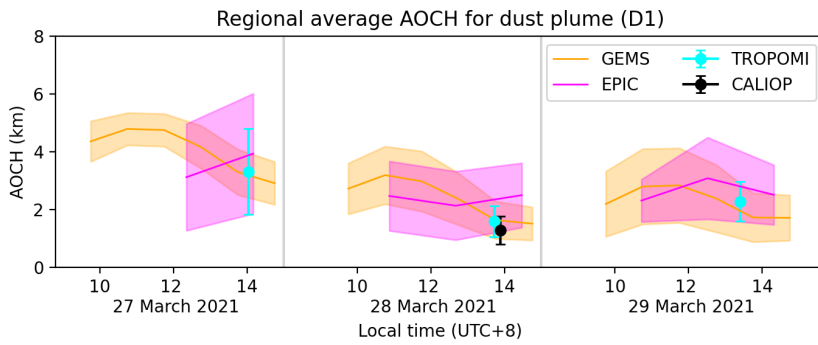
Figure 11. Time series plot of regional average AOCH for a dust plume on 28 March 2021 (D1). AOCH of GEMS, TROPOMI, and EPIC is represented as orange, cyan, and magenta, respectively. The lines and shadows indicate the mean and the standard deviation, respectively. CALIOP AOCH is represented by the black error bar. GEMS AEH, EPIC AOCH, and TROPOMI AOCH are all converted to the CALIOP AOCH definition.

4.2 Smoke plume case

Figure 12 displays ALH retrievals from GEMS with TROPOMI and EPIC for one of the selected smoke case on April 17, 2023 (B6). The first row displays GEMS AOCH, converted from GEMS AEH to match the EPIC/TROPOMI AOCH definition. The second row shows EPIC and TROPOMI AOCH aligned with the closest GEMS measurement time. In addition, AOD and UVAI maps are provided in Fig. S13. This particular case is a smoke event in Southeast Asia, with the identified smoke plume situated predominantly over the northern areas of Laos and Thailand, shown in the central part of the domain (20º N, 100º E) indicated by the black star on Fig. 12a. Over the previous decades, the air quality in Southeast Asia has been periodically affected by the transboundary smoke and haze issue, primarily linked to slash-and-burn agriculture and land clearing practices, particularly during the dry season (Shi et al., 2014; Chang and Song, 2010). Focusing on the smoke plume that can be identified from EPIC/TROPOMI AOCH retrieval for absorbing aerosols, GEMS AOCH ranges from 3 to 5 km, while EPIC and TROPOMI consistently show values predominantly exceeding 4 km over land. The decrease in EPIC AOCH spatial coverage throughout the day, coupled with an increase in AOCH values (Fig 12i & j), indicates the dissipation process of the smoke plume.
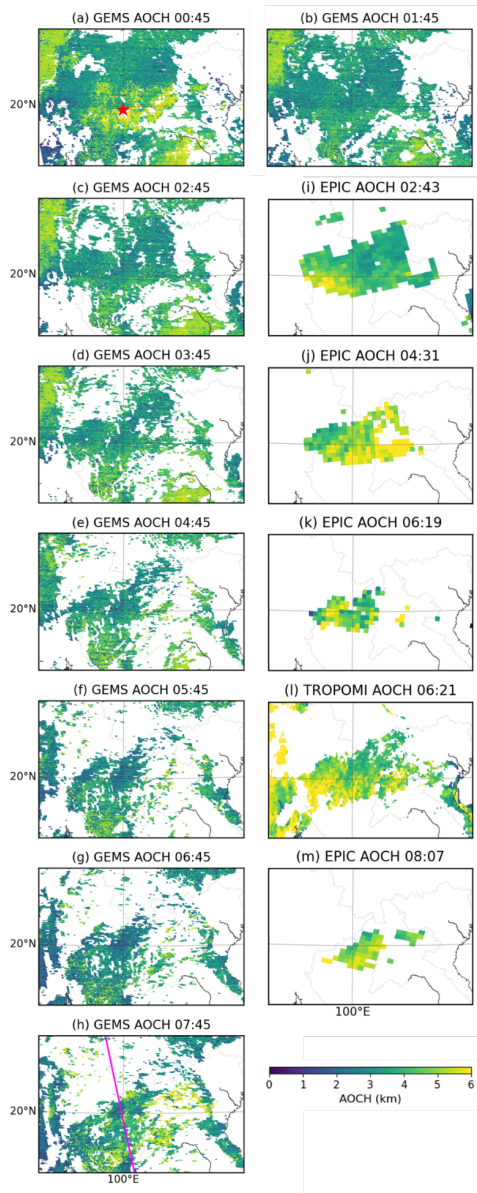
Figure 12. The first row (a – f) shows hourly GEMS AOCH (GEMS AEH adjusted to EPIC/TROPOMI AOCH definition) from (a) 00:45 to (f) 07:45 (UTC). Second row (g – i) EPIC and TROPOMI AOCH aligned on the nearest GEMS measurement times for a smoke plume event on 17 April 2023. The magenta line on the GEMS maps in the first column indicates the CALIOP ground tracks, which have the closest observation times with GEMS. The red star indicates the smoke plume area.
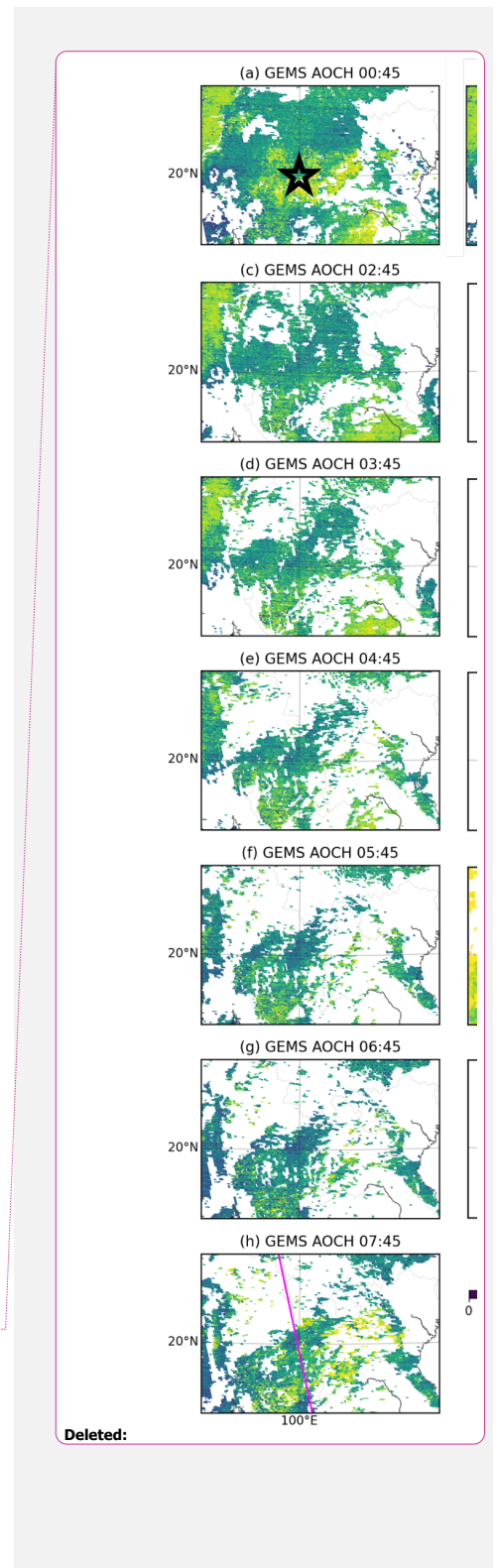
Figure 13 presents a comparison with CALIOP AOCH, specifically highlighting the northern regions of Laos and Thailand where the smoke plume is detected along the CALIOP ground track. GEMS AEH and EPIC/TROPOMI AOCH values have been converted to the CALIOP AOCH definition. GEMS and CALIOP AOCH show comparability within the range

815 of 2-4 km, as evidenced by a smaller RMSE of 0.75 km. On the contrary, EPIC and TROPOMI ALH values are approximately 2 km higher than CALIOP ALH, yet they display similar vertical distribution patterns of the smoke plume over the region of 19-20º N. This suggests that EPIC and TROPOMI AOCH retrievals exhibit a systematic positive bias for aerosols over Southeast Asia, indicating the potential need for tuning in the related smoke model, including surface reflectance and aerosol properties like size distribution, refractive index, single scattering albedo. In general, GEMS

820 demonstrates comparability with CALIOP AOCH, whereas both EPIC and TROPOMI ALH tend to overestimate.
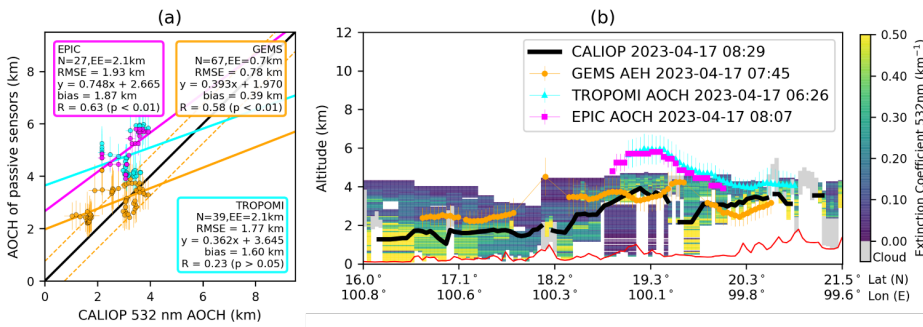
Figure 13. Same as Figure 10 but for a smoke case over Southeast Asia on 17 April 2023.

825 In Fig. 14, we present the regional averaged ALH for absorbing aerosols for this smoke case. UVAI thresholds are chosen to facilitate the comparison of ALH among GEMS, EPIC, and TROPOMI, ensuring a consistent focus on regions with comparable coverage of absorbing aerosols. UVAI thresholds for GEMS, TROPOMI, and EPIC, are set as 3, 1.5, and 2, respectively. Detailed regional ALH map from all products are provided in Fig. S14. Notably, since the CALIOP product is included, all GEMS AEH and EPIC/TROPOMI AOCH values have been converted to the CALIOP AOCH definition.

830 In contrast to the dust case discussed in Section 4.1, this smoke plume shows little diurnal variation throughout the day according to GEMS, and an overall slight increase observed by EPIC. Post 5 UTC time, GEMS and EPIC exhibit similar patterns, yet EPIC consistently registers ALH values approximately 2 km higher throughout the day. While the observation times of CALIOP do not align with the consecutive data of GEMS, the regional average of CALIOP AOCH falls within the range of GEMS AOCH. Additionally, the regional mean of TROPOMI AOCH is higher than that of GEMS but lower

835 than EPIC for this smoke plume.
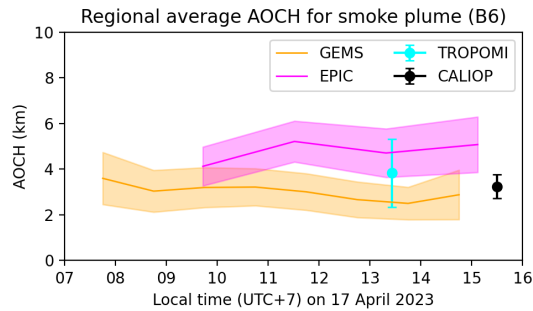
Figure 14. Time series plot of regional average AOCH for a smoke plume on 17 April 2023. AOCH of GEMS, TROPOMI, and EPIC is represented as orange, cyan, and magenta, respectively. The lines and shadows indicate the mean and the standard deviation, respectively. CALIOP AOCH is represented by the black error bar. GEMS AEH, EPIC AOCH, and TROPOMI AOCH are all converted to CALIOP AOCH definition.

5 Conclusion and discussion

Aerosol vertical distribution is important for assessing aerosol climate impact, surface air quality, and remote sensing of aerosols. In this study, we compared multiple aerosol layer height (ALH) products from satellite platforms of GEMS, EPIC, and TROPOMI that use oxygen (or oxygen dimer) absorption bands, specifically O_2-O_2 band for GEMS, and O_2 A and B bands for TROPOMI and EPIC. Several dust and smoke plume cases over different regions in Asia covered by the field of regard of GEMS were selected for comparison. Adjustments have been made to account for the inherent variations in the definitions of ALH among different products, ensuring an apple-to-apple comparison.

As part of the ALH retrieval evaluation, we also evaluated the AOD retrievals from GEMS, EPIC and TROPOMI with AERONET AOD and compared the UVAI among these satellite platforms. Compared with AERONET, GEMS AOD at 443 nm demonstrates a strong positive correlation in both dust (R = 0.9) and smoke cases (R = 0.88). Discrepancies arise at 680 nm for dust cases, indicating potential inaccuracies in GEMS dust aerosol model. TROPOMI and EPIC tend to overestimate AOD in dust cases due to underestimated surface reflectance. The inaccuracies in the GEMS dust aerosol model contribute to the significant differences in GEMS AOD compared to TROPOMI and EPIC. Additionally, the differences are compounded by other causes including potential inaccuracies in surface reflectance in TROPOMI and EPIC. In addition, GEMS UVAI is consistently larger than TROPOMI UVAI, by 1.2, whereas it shows a better agreement with EPIC UVAI with a smaller bias of 0.32.

The results indicate that EPIC and TROPOMI generally overestimate ALH values compared to CALIOP, with RMSE values of 1.25 km and 1.31 km, respectively. In contrast, GEMS demonstrates a minimal bias and the lowest RMSE of 0.75 km, although it exhibits a slightly lower correlation with CALIOP (R=0.64). When valid data from all sensors are present, stronger correlations (R > 0.9) with CALIOP ALH are observed across all passive sensors, however, TROPOMI and EPIC still tend to overestimate ALH. Categorizing GEMS aerosol retrievals based on a UVAI threshold of 3 revealed better overall agreement with CALIOP ALH for aerosols with UVAI ≥ 3. While comparing GEMS with EPIC and

TROPOMI, a narrower range in GEMS AEH was seen due in part to limitations in its algorithm LUT, within the range of 0.2 to 5 km, while EPIC and TROPOMI had LUTs extending from 0 to 9 km.

The diurnal pattern of EPIC AOCH values shows a morning ascent (~ 4.5 km) and declining after noon, while GEMS remains relatively stable until a more pronounced descent in the late morning and early afternoon to below 3 km. MERRA-2 data analysis indicates a similar diurnal variation between PBLH and MERRA-2 AOCH, suggesting that when most aerosols are within the PBL, their diurnal variation is affected by the PBL process. The validation of the diurnal variation of ALH is very challenging due to limited spatial and temporal resolution in active remote sensing measurements and potential artifacts in passive remote sensing data.

Lastly, we presented a detailed analysis on both a dust case and a smoke case to compare differences in spatial and vertical distribution of ALH products, along with diurnal variations. GEMS, with its higher temporal resolution, captured diurnal variations of the dust plume, while EPIC showed the highest correlation (R = 0.74) and TROPOMI had the lowest RMSE (0.33 km) with CALIOP. In the smoke plume case, both EPIC and TROPOMI exhibited a consistent positive bias of over 1.5 km compared to CALIOP, likely due to differences in surface reflectance and aerosol property assumptions. Overall, the passive sensors demonstrated consistent trends in ALH, but the hourly observations of GEMS provide valuable insights into the diurnal variations of ALH from individual dust and smoke plumes, which limited observations from other sensors could not fully capture.

In conclusion, our comprehensive analysis provides a thorough evaluation of the performance and comparative assessment of ALH, AOD, and UVAI retrievals from GEMS, EPIC, and TROPOMI. The comparison of the ALH definition among different sensors highlights the need for standardization, ensuring a consistent basis for comparisons. Results from this study help enhance our understanding of aerosol plume characteristics, overcoming challenges associated with previously difficult aspects such as the comparison of ALH diurnal variations. Furthermore, we offer insights for future ALH product development by identifying and addressing the limitations in inputs from each retrieval algorithm, such as the impact of aerosol models and surface reflectance.

Appendix A: List of acronyms

AE	Angstrom exponent
AEH	Aerosol effective height
AERONET	AErosol RObotic NETwork
ALH	Aerosol layer height
AOCH	Aerosol optical central height
AOCH	Aerosol optical central height
AOD	Aerosol optical depth
CALIOP	Cloud-Aerosol Lidar with Orthogonal Polarization
CALIPSO	Cloud-Aerosol Lidar and Infrared Pathfinder Satellite Observation
CLARS-FTS	California Laboratory for Atmospheric Remote Sensing Fourier Transform Spectrometer
DOAS	Differential optical absorption spectroscopy
DOFS	Degrees of freedom for signal

DSCOVR	Deep Space Climate Observatory
EPIC	Earth Polychromatic Imaging Camera
GEMS	Geostationary Environment Monitoring Spectrometer
HAF	Highly absorbing fine
IR	Infrared
LST	Local solar time
LUT	Look-up table
MBE	Mean bias error
MERRA-2	Modern-Era Retrospective Analysis for Research and Applications, Version 2
MPLNET	NASA Micro-Pulse Lidar Network
NA	Non-absorbing
NIR	Near-infrared
OMI	Ozone Monitoring Instrument
PBL(H)	Planetary boundary layer (height)
PM	Particulate matter
RMSE	Root mean square error
SCD	Slant column density
SCIAMACHY	Scanning Imaging Absorption spectroMeter for Atmospheric CHartographY
SNR	Signal-to-noise ratio
SSA	Single scattering albedo
SWIR	Shortwave infrared
SZA	Solar zenith angle
TOA	Top of atmosphere
TOMS	Total Ozone Mapping Spectrometer
TROPOMI	TROPOspheric Monitoring Instrument
UV	Ultra-violet
UVAI	UV aerosol index
VisAI	Visible aerosol index

Code availability

Aerosol layer height and aerosol optical depth analysis codes are available at https://doi.org/10.5281/zenodo.10408292.

Data availability

990 TROPOMI AOCH dataset used in this study can be found at http://doi.org/10.5281/zenodo.10407271. EPIC level 2 AOCH data can be found at https://opendap.larc.nasa.gov/opendap/DSCOVR/EPIC/L2_AOCH_01/contents.html. GEMS L2 AEH V2.0 and AERAOD V2.0 can be downloaded from the Environmental Satellite Center website (https://nesc.nier.go.kr/en/html/datasvc/index.do). CALIOP level 2 data are from https://asdc.larc.nasa.gov/data/. Earthdata registration is required for the access to the CALIOP level 2 data.

995 **Author contribution**

HK performed data curation, formal analysis, visualization, and writing most of the original draft. XC was responsible for conceptualization, formal analysis, methodology, writing parts of the original draft, and supervision. XC also provided TROPOMI AOCH data and ZL provided the EPIC AOCH data. JW provided comments on the research design and supervision. MZ contributed on formal analysis and GRC provided comments on writing focus and structure. SSP provided 1000 GEMS AEH V2.0 data. All authors including JK provided comments and edited the manuscript.

Competing interests

Jun Wang is a member of the editorial board of *Atmospheric Measurement Techniques*.

Acknowledgements

This was supported by NASA EPIC/DSCOVR science team program (grant 80NSSC22K0503), NASA SERVIR grant 1005 (80NSSC23K0244), NOAA's GEO-XO-ACX concept evaluation program (contracts 1305M322PNRMT0542, and 1305M323PNRMN0450, grant NA23OAR4310303), and NOAA's Climate Program Office Earth's Radiation Budget (ERB), Atmospheric Chemistry, Carbon Cycle, & Climate (AC4), and Climate Variability & Predictability (CVP) Programs (grant NA23OAR4310302, NA23OAR4310303, and NA23OAR4310304), and Improving modeling capabilities in Asia through forecasting and analysis that integrates satellite, surface based air quality measurements and models in 1010 support of Asian-AQ (grant 80NSSC23K0820). We thank the National Institute of Environmental Research of South Korea for providing GEMS satellite data. We acknowledge the public availability of CALIOP Level 2 aerosol profile data from the NASA Langley Research Center Atmospheric Science Data Center. We thank all Principal Investigators, Co-Principal Investigators and their staff for establishing and maintaining the AERONET sites used in this investigation.

References

1015 Babu, S. S., Moorthy, K. K., Manchanda, R. K., Sinha, P. R., Satheesh, S. K., Vajja, D. P., Srinivasan, S., and Kumar, V. H. A.: Free tropospheric black carbon aerosol measurements using high altitude balloon: Do BC layers build "their own homes" up in the atmosphere?, Geophys Res Lett, 38, https://doi.org/10.1029/2011gl046654, 2011.

Chang, D. and Song, Y.: Estimates of biomass burning emissions in tropical Asia based on satellite-derived data, Atmos. Chem. Phys., 10, 2335-2351, https://doi.org/10.5194/acp-10-2335-2010, 2010.

1020 Chen, X., Xu, X. G., Wang, J., and Diner, D. J.: Can multi-angular polarimetric measurements in the oxygen-A and B bands improve the retrieval of aerosol vertical distribution?, J Quant Spectrosc Ra, 270, https://doi.org/10.1016/j.jqsrt.2021.107679, 2021a.

Chen, X., Wang, J., Xu, X. G., Zhou, M., Zhang, H. X., Garcia, L. C., Colarco, P. R., Janz, S. J., Yorks, J., McGill, M., Reid, J. S., de Graaf, M., and Kondragunta, S.: First retrieval of absorbing aerosol height over dark target using TROPOMI oxygen B band:

Algorithm development and application for surface particulate matter estimates, Remote Sensing of Environment, 265, 18, https://doi.org/10.1016/j.rse.2021.112674, 2021b.

Chimot, J., Veefkind, J. P., Vlemmix, T., de Haan, J. F., Amiridis, V., Proestakis, E., Marinou, E., and Levelt, P. F.: An exploratory study on the aerosol height retrieval from OMI measurements of the 477 nm O-2-O-2 spectral band using a neural network approach, Atmos Meas Tech, 10, 783-809, https://doi.org/10.5194/amt-10-783-2017, 2017.

Cho, Y., Kim, J., Go, S., Kim, M., Lee, S., Kim, M., Chong, H., Lee, W. J., Lee, D. W., Torres, O., and Park, S. S.: First Atmospheric Aerosol Monitoring Results from Geostationary Environment Monitoring Spectrometer (GEMS) over Asia[preprint], https://doi.org/10.5194/amt-2023-221, 23 October 2023.

Christian, K., Wang, J., Ge, C., Peterson, D., Hyer, E., Yorks, J., and McGill, M.: Radiative Forcing and Stratospheric Warming of Pyrocumulonimbus smoke Aerosols: First Modeling Results With Multisensor (EPIC, CALIPSO, AND CATS) Views from Space, Geophys Res Lett, 46, 10061-10071, https://doi.org/10.1029/2019gl082360, 2019.

Ding, S. G., Wang, J., and Xu, X. G.: Polarimetric remote sensing in oxygen A and B bands: sensitivity study and information content analysis for vertical profile of aerosols, Atmos Meas Tech, 9, 2077-2092, https://doi.org/10.5194/amt-9-2077-2016, 2016.

Geddes, A. and Bösch, H.: Tropospheric aerosol profile information from high-resolution oxygen A-band measurements from space, Atmos Meas Tech, 8, 859-874, https://doi.org/10.5194/amt-8-859-2015, 2015.

Geogdzhayev, I. V. and Marshak, A.: Calibration of the DSCOVR EPIC visible and NIR channels using MODIS Terra and Aqua data and EPIC lunar observations, Atmos. Meas. Tech., 11, 359-368, https://doi.org/10.5194/amt-11-359-2018, 2018.

Holben, B. N., Eck, T. F., Slutsker, I., Tanré, D., Buis, J. P., Setzer, A., Vermote, E., Reagan, J. A., Kaufman, Y. J., Nakajima, T., Lavenu, F., Jankowiak, I., and Smirnov, A.: AERONET—A Federated Instrument Network and Data Archive for Aerosol Characterization, Remote Sensing of Environment, 66, 1-16, https://doi.org/https://doi.org/10.1016/S0034-4257(98)00031-5, 1998.

Kang, M., Ahn, M.-H., Liu, X., Jeong, U., and Kim, J.: Spectral Calibration Algorithm for the Geostationary Environment Monitoring Spectrometer (GEMS), Remote Sens-Basel, 12, 2846, 2020.

Kim, J., Jeong, U., Ahn, M. H., Kim, J. H., Park, R. J., Lee, H., Song, C. H., Choi, Y. S., Lee, K. H., Yoo, J. M., Jeong, M. J., Park, S. K., Lee, K. M., Song, C. K., Kim, S. W., Kim, Y. J., Kim, S. W., Kim, M., Go, S., Liu, X., Chance, K., Chan Miller, C., Al-Saadi, J., Veihelmann, B., Bhartia, P. K., Torres, O., Abad, G. G., Haffner, D. P., Ko, D. H., Lee, S. H., Woo, J. H., Chong, H., Park, S. S., Nicks, D., Choi, W. J., Moon, K. J., Cho, A., Yoon, J., Kim, S. K., Hong, H., Lee, K., Lee, H., Lee, S., Choi, M., Veefkind, P., Levelt, P. F., Edwards, D. P., Kang, M., Eo, M., Bak, J., Baek, K., Kwon, H. A., Yang, J., Park, J., Han, K. M., Kim, B. R., Shin, H. W., Choi, H., Lee, E., Chong, J., Cha, Y., Koo, J. H., Irie, H., Hayashida, S., Kasai, Y., Kanaya, Y., Liu, C., Lin, J., Crawford, J. H., Carmichael, G. R., Newchurch, M. J., Lefer, B. L., Herman, J. R., Swap, R. J., Lau, A. K. H., Kurosu, T. P., Jaross, G., Ahlers, B., Dobber, M., McElroy, C. T., and Choi, Y.: New Era of Air Quality Monitoring from Space: Geostationary Environment Monitoring Spectrometer (GEMS), B Am Meteorol Soc, 101, E1-E22, https://doi.org/10.1175/bams-d-18-0013.1, 2020.

Kim, M., Kim, J., Lim, H., Lee, S., Cho, Y., Yeo, H., and Kim, S. W.: Exploring geometrical stereoscopic aerosol top height retrieval from geostationary satellite imagery in East Asia, Atmos Meas Tech, 16, 2673-2690, https://doi.org/10.5194/amt-16-2673-2023, 2023.

Kim, M., Kim, J., Torres, O., Ahn, C., Kim, W., Jeong, U., Go, S., Liu, X., Moon, K. J., and Kim, D. R.: Optimal Estimation-Based Algorithm to Retrieve Aerosol Optical Properties for GEMS Measurements over Asia, Remote Sens-Basel, 10, https://doi.org/10.3390/rs10020162, 2018.

Kipling, Z., Stier, P., Schwarz, J. P., Perring, A. E., Spackman, J. R., Mann, G. W., Johnson, C. E., and Telford, P. J.: Constraints on aerosol processes in climate models from vertically-resolved aircraft observations of black carbon, Atmos Chem Phys, 13, 5969-5986, https://doi.org/10.5194/acp-13-5969-2013, 2013.

Kipling, Z., Stier, P., Johnson, C. E., Mann, G. W., Bellouin, N., Bauer, S. E., Bergman, T., Chin, M., Diehl, T., Ghan, S. J., Iversen, T., Kirkevag, A., Kokkola, H., Liu, X. H., Luo, G., van Noije, T., Pringle, K. J., von Salzen, K., Schulz, M., Seland, O., Skeie, R. B., Takemura, T., Tsigaridis, K., and Zhang, K.: What controls the vertical distribution of aerosol? Relationships between process sensitivity in HadGEM3-UKCA and inter-model variation from AeroCom Phase II, Atmos Chem Phys, 16, 2221-2241, https://doi.org/10.5194/acp-16-2221-2016, 2016.

Kleipool, Q., Ludewig, A., Babić, L., Bartstra, R., Braak, R., Dierssen, W., Dewitte, P. J., Kenter, P., Landzaat, R., Leloux, J., Loots, E., Meijering, P., van der Plas, E., Rozemeijer, N., Schepers, D., Schiavini, D., Smeets, J., Vacanti, G., Vonk, F., and Veefkind, P.: Pre-launch calibration results of the TROPOMI payload on-board the Sentinel-5 Precursor satellite, Atmos. Meas. Tech., 11, 6439-6479, https://doi.org/10.5194/amt-11-6439-2018, 2018.

Koch, D. and Del Genio, A. D.: Black carbon semi-direct effects on cloud cover: review and synthesis, Atmos Chem Phys, 10, 7685-7696, https://doi.org/10.5194/acp-10-7685-2010, 2010.

Koffi, B., Schulz, M., Breon, F. M., Dentener, F., Steensen, B. M., Griesfeller, J., Winker, D., Balkanski, Y., Bauer, S. E., Bellouin, N., Berntsen, T., Bian, H. S., Chin, M., Diehl, T., Easter, R., Ghan, S., Hauglustaine, D. A., Iversen, T., Kirkevag, A., Liu, X. H., Lohmann, U., Myhre, G., Rasch, P., Seland, O., Skeie, R. B., Steenrod, S. D., Stier, P., Tackett, J., Takemura, T., Tsigaridis, K., Vuolo, M. R., Yoon, J., and Zhang, K.: Evaluation of the aerosol vertical distribution in global aerosol models

through comparison against CALIOP measurements: AeroCom phase II results, J Geophys Res-Atmos, 121, 7254-7283, https://doi.org/10.1002/2015jd024639, 2016.

Kokhanovsky, A. A. and Rozanov, V. V.: The determination of dust cloud altitudes from a satellite using hyperspectral measurements in the gaseous absorption band, Int J Remote Sens, 31, 2729-2744, https://doi.org/10.1080/01431160903085644, 2010.

1100 Lee, L., Zhang, J., Reid, J. S., and Yorks, J. E.: Investigation of CATS aerosol products and application toward global diurnal variation of aerosols, Atmos. Chem. Phys., 19, 12687-12707, https://doi.org/10.5194/acp-19-12687-2019, 2019.

Lu, Z. D., Wang, J., Xu, X. G., Chen, X., Kondragunta, S., Torres, O., Wilcox, E. M., and Zeng, J.: Hourly Mapping of the Layer Height of Thick Smoke Plumes Over the Western US in 2020 Severe Fire Season, Front. Remote Sens., 2, 13, https://doi.org/10.3389/frsen.2021.766628, 2021.

1105 Lu, Z. D., Wang, J., Chen, X., Zeng, J., Wang, Y., Xu, X. G., Christian, K. E., Yorks, J. E., Nowottnick, E. P., Reid, J. S., and Xian, P.: First Mapping of Monthly and Diurnal Climatology of Saharan Dust Layer Height Over the Atlantic Ocean From EPIC/DSCOVR in Deep Space, Geophys Res Lett, 50, 10, https://doi.org/10.1029/2022gl102552, 2023.

Marshak, A., Herman, J., Szabo, A., Blank, K., Carn, S., Cede, A., Geogdzhayev, I., Huang, D., Huang, L. K., Knyazikhin, Y., Kowalewski, M., Krotkov, N., Lyapustin, A., McPeters, R., Meyer, K. G., Torres, O., and Yang, Y. K.: Earth Observations
1110 from Dscovr Epic Instrument, B Am Meteorol Soc, 99, 1829-1850, https://doi.org/10.1175/Bams-D-17-0223.1, 2018.

Muller, J. P., Denis, M. A., Dundas, R. D., Mitchell, K. L., Naud, C., and Mannstein, H.: Stereo cloud-top heights and cloud fraction retrieval from ATSR-2, Int J Remote Sens, 28, 1921-1938, https://doi.org/10.1080/01431160601030975, 2007.

Nanda, S., de Graaf, M., Veefkind, J. P., Sneep, M., ter Linden, M., Sun, J. Y. T., and Levelt, P. F.: A first comparison of TROPOMI aerosol layer height (ALH) to CALIOP data, Atmos Meas Tech, 13, 3043-3059, https://doi.org/10.5194/amt-13-3043-2020,
1115 2020.

Park, S. S., Kim, J., Lee, H., Torres, O., Lee, K. M., and Lee, S. D.: Utilization of O-4 slant column density to derive aerosol layer height from a space-borne UV-visible hyperspectral sensor: sensitivity and case study, Atmos Chem Phys, 16, 1987-2006, https://doi.org/10.5194/acp-16-1987-2016, 2016.

Park, S. S., Kim, J., Cho, Y., Lee, H., Park, J., Lee, D. W., Lee, W. J., and Kim, D. R.: Retrieval Algorithm for Aerosol Effective Height
1120 from the Geostationary Environment Monitoring Spectrometer (GEMS)[preprint], https://doi.org/10.5194/amt-2023-136, 04 July 2023.

Peterson, D., Hyer, E., and Wang, J.: Quantifying the potential for high-altitude smoke injection in the North American boreal forest using the standard MODIS fire products and subpixel-based methods, J Geophys Res-Atmos, 119, 3401-3419, https://doi.org/10.1002/2013jd021067, 2014.

1125 Pierangelo, C., Chedin, A., Heilliette, S., Jacquinet-Husson, N., and Armante, R.: Dust altitude and infrared optical depth from AIRS, Atmos Chem Phys, 4, 1813-1822, https://doi.org/10.5194/acp-4-1813-2004, 2004.

Rao, L. L., Xu, J., Efremenko, D. S., Loyola, D. G., and Doicu, A.: Hyperspectral Satellite Remote Sensing of Aerosol Parameters: Sensitivity Analysis and Application to TROPOMI/S5P, Front. Environ. Sci., 9, 16, https://doi.org/10.3389/fenvs.2021.770662, 2022.

1130 Reid, J. S., Kinney, J. E., Westphal, D. L., Holben, B. N., Welton, E. J., Tsay, S.-C., Eleuterio, D. P., Campbell, J. R., Christopher, S. A., Colarco, P. R., Jonsson, H. H., Livingston, J. M., Maring, H. B., Meier, M. L., Pilewskie, P., Prospero, J. M., Reid, E. A., Remer, L. A., Russell, P. B., Savoie, D. L., Smirnov, A., and Tanré, D.: Analysis of measurements of Saharan dust by airborne and ground-based remote sensing methods during the Puerto Rico Dust Experiment (PRIDE), Journal of Geophysical Research: Atmospheres, 108, https://doi.org/https://doi.org/10.1029/2002JD002493, 2003.

1135 Shi, Y. S., Sasai, T., and Yamaguchi, Y.: Spatio-temporal evaluation of carbon emissions from biomass burning in Southeast Asia during the period 2001-2010, Ecol Model, 272, 98-115, https://doi.org/10.1016/j.ecolmodel.2013.09.021, 2014.

Spurr, R. and Christi, M.: On the generation of atmospheric property Jacobians from the (V)LIDORT linearized radiative transfer models, J Quant Spectrosc Ra, 142, 109-115, https://doi.org/10.1016/j.jqsrt.2014.03.011, 2014.

Stein Zweers, D. C.: TROPOMI ATBD of the UV aerosol index, S5P-KNMI-L2-0008-RP:
1140 https://sentinel.esa.int/documents/247904/2476257/Sentinel-5P-TROPOMI-ATBD-UV-Aerosol-Index.pdf, last access: 17 December 2023.

Torres, O., Bhartia, P. K., Herman, J. R., Ahmad, Z., and Gleason, J.: Derivation of aerosol properties from satellite measurements of backscattered ultraviolet radiation: Theoretical basis, J Geophys Res-Atmos, 103, 17099-17110, https://doi.org/10.1029/98jd00900, 1998.

1145 Torres, O., Tanskanen, A., Veihelmann, B., Ahn, C., Braak, R., Bhartia, P. K., Veefkind, P., and Levelt, P.: Aerosols and surface UV products from Ozone Monitoring Instrument observations: An overview, J Geophys Res-Atmos, 112, https://doi.org/10.1029/2007jd008809, 2007.

Vandenbussche, S., Kochenova, S., Vandaele, A. C., Kumps, N., and De Maziere, M.: Retrieval of desert dust aerosol vertical profiles from IASI measurements in the TIR atmospheric window, Atmos Meas Tech, 6, 2577-2591, https://doi.org/10.5194/amt-6-
1150 2577-2013, 2013.

Wang, J. and Christopher, S. A.: Intercomparison between satellite-derived aerosol optical thickness and PM2.5 mass: Implications for air quality studies, Geophys Res Lett, 30, https://doi.org/10.1029/2003gl018174, 2003.

Wang, J. and Christopher, S. A.: Mesoscale modeling of Central American smoke transport to the United States: 2. Smoke radiative impact on regional surface energy budget and boundary layer evolution, J Geophys Res-Atmos, 111, https://doi.org/10.1029/2005jd006720, 2006.

Wang, J., Christopher, S. A., Nair, U. S., Reid, J. S., Prins, E. M., Szykman, J., and Hand, J. L.: Mesoscale modeling of Central American smoke transport to the United States: 1. "Top-down" assessment of emission strength and diurnal variation impacts, J Geophys Res-Atmos, 111, https://doi.org/10.1029/2005jd006416, 2006.

Wang, J., Ge, C., Yang, Z. F., Hyer, E. J., Reid, J. S., Chew, B. N., Mahmud, M., Zhang, Y. X., and Zhang, M. G.: Mesoscale modeling of smoke transport over the Southeast Asian Maritime Continent: Interplay of sea breeze, trade wind, typhoon, and topography, Atmos Res, 122, 486-503, https://doi.org/10.1016/j.atmosres.2012.05.009, 2013.

Wang, J., Roudini, S., Hyer, E. J., Xu, X. G., Zhou, M., Garcia, L. C., Reid, J. S., Peterson, D. A., and da Silva, A. M.: Detecting nighttime fire combustion phase by hybrid application of visible and infrared radiation from Suomi NPP VIIRS, Remote Sensing of Environment, 237, 14, https://doi.org/10.1016/j.rse.2019.111466, 2020.

Wendisch, M., Hellmuth, O., Ansmann, A., Heintzenberg, J., Engelmann, R., Althausen, D., Eichler, H., Wuller, D., Hu, M., Zhang, Y., and Mao, J.: Radiative and dynamic effects of absorbing aerosol particles over the Pearl River Delta, China, Atmos Environ, 42, 6405-6416, https://doi.org/10.1016/j.atmosenv.2008.02.033, 2008.

Winker, D. M., Tackett, J. L., Getzewich, B. J., Liu, Z., Vaughan, M. A., and Rogers, R. R.: The global 3-D distribution of tropospheric aerosols as characterized by CALIOP, Atmos Chem Phys, 13, 3345-3361, https://doi.org/10.5194/acp-13-3345-2013, 2013.

Winker, D. M., Vaughan, M. A., Omar, A., Hu, Y., Powell, K. A., Liu, Z., Hunt, W. H., and Young, S. A.: Overview of the CALIPSO Mission and CALIOP Data Processing Algorithms, Journal of Atmospheric and Oceanic Technology, 26, 2310-2323, https://doi.org/https://doi.org/10.1175/2009JTECHA1281.1, 2009.

Wu, L. H., Hasekamp, O., van Diedenhoven, B., Cairns, B., Yorks, J. E., and Chowdhary, J.: Passive remote sensing of aerosol layer height using near-UV multiangle polarization measurements, Geophys Res Lett, 43, 8783-8790, https://doi.org/10.1002/2016gl069848, 2016.

Xu, X., Wang, J., Wang, Y., and Kokhanovsky, A.: Chapter 1 - Passive Remote Sensing of Aerosol Height, in: Remote Sensing of Aerosols, Clouds, and Precipitation, edited by: Tanvir Islam, Y. H., Alexander Kokhanovsky, Jun Wang, Elsevier, Cambridge, MA, 1-22, https://doi.org/10.1016/B978-0-12-810437-8.00001-3, 2018.

Xu, X. G., Wang, J., Wang, Y., Zeng, J., Torres, O., Reid, J. S., Miller, S. D., Martins, J. V., and Remer, L. A.: Detecting layer height of smoke aerosols over vegetated land and water surfaces via oxygen absorption bands: hourly results from EPIC/DSCOVR in deep space, Atmos Meas Tech, 12, 3269-3288, https://doi.org/10.5194/amt-12-3269-2019, 2019.

Xu, X. G., Wang, J., Wang, Y., Zeng, J., Torres, O., Yang, Y. K., Marshak, A., Reid, J., and Miller, S.: Passive remote sensing of altitude and optical depth of dust plumes using the oxygen A and B bands: First results from EPIC/DSCOVR at Lagrange-1 point, Geophys Res Lett, 44, 7544-7554, https://doi.org/10.1002/2017gl073939, 2017.

Yang, Z. F., Wang, J., Ichoku, C., Hyer, E., and Zeng, J.: Mesoscale modeling and satellite observation of transport and mixing of smoke and dust particles over northern sub-Saharan African region, J Geophys Res-Atmos, 118, 12139-12157, https://doi.org/10.1002/2013jd020644, 2013.

Zeng, J., Han, Q. Y., and Wang, J.: High-spectral resolution simulation of polarization of skylight: Sensitivity to aerosol vertical profile, Geophys Res Lett, 35, https://doi.org/10.1029/2008gl035645, 2008.

Zhang, L., Li, Q. B., Gu, Y., Liou, K. N., and Meland, B.: Dust vertical profile impact on global radiative forcing estimation using a coupled chemical-transport-radiative-transfer model, Atmos Chem Phys, 13, 7097-7114, https://doi.org/10.5194/acp-13-7097-2013, 2013.

Page 1: [1] Deleted   **Kim, Hyerim**   **10/3/24 9:38:00 PM**

Page 1: [2] Deleted   **Kim, Hyerim**   **10/3/24 9:38:00 PM**

Page 26: [3] Deleted   **Kim, Hyerim**   **10/3/24 9:38:00 PM**

Page 27: [4] Formatted   **Kim, Hyerim**   **10/3/24 9:38:00 PM**

Font: Times New Roman

Page 27: [5] Formatted   **Kim, Hyerim**   **10/3/24 9:38:00 PM**

Left, Line spacing: single

Page 27: [6] Formatted Table   **Kim, Hyerim**   **10/3/24 9:38:00 PM**

Formatted Table

Page 27: [7] Formatted   **Kim, Hyerim**   **10/3/24 9:38:00 PM**

Font: Times New Roman, English (US)

Page 27: [8] Formatted   **Kim, Hyerim**   **10/3/24 9:38:00 PM**

Font: Times New Roman

Page 27: [8] Formatted   **Kim, Hyerim**   **10/3/24 9:38:00 PM**

Font: Times New Roman

Page 27: [9] Formatted   **Kim, Hyerim**   **10/3/24 9:38:00 PM**

Font: Times New Roman

Page 27: [10] Formatted   **Kim, Hyerim**   **10/3/24 9:38:00 PM**

Left, Line spacing: single

Page 27: [11] Formatted   **Kim, Hyerim**   **10/3/24 9:38:00 PM**

Font: Times New Roman, English (US)

Page 27: [12] Formatted   **Kim, Hyerim**   **10/3/24 9:38:00 PM**

Font: Times New Roman

Page 27: [12] Formatted   **Kim, Hyerim**   **10/3/24 9:38:00 PM**

Font: Times New Roman

Page 27: [13] Formatted   **Kim, Hyerim**   **10/3/24 9:38:00 PM**

Font: Times New Roman

Page 27: [14] Formatted   **Kim, Hyerim**   **10/3/24 9:38:00 PM**

Left, Line spacing: single

Page 27: [15] Formatted   **Kim, Hyerim**   **10/3/24 9:38:00 PM**

Font: Times New Roman, English (US)

Page 27: [16] Formatted   Kim, Hyerim   10/3/24 9:38:00 PM

Font: Times New Roman

Page 27: [16] Formatted   Kim, Hyerim   10/3/24 9:38:00 PM

Font: Times New Roman

Page 27: [17] Formatted   Kim, Hyerim   10/3/24 9:38:00 PM

Font: 10 pt, Font color: Auto

Page 27: [18] Formatted   Kim, Hyerim   10/3/24 9:38:00 PM

Left, Line spacing: single

Page 27: [19] Formatted   Kim, Hyerim   10/3/24 9:38:00 PM

English (US)

Page 27: [20] Formatted   Kim, Hyerim   10/3/24 9:38:00 PM

Font: 10 pt, Font color: Auto

Page 27: [20] Formatted   Kim, Hyerim   10/3/24 9:38:00 PM

Font: 10 pt, Font color: Auto

Page 27: [21] Formatted   Kim, Hyerim   10/3/24 9:38:00 PM

Font: 10 pt, Font color: Auto

Page 27: [22] Formatted   Kim, Hyerim   10/3/24 9:38:00 PM

Left, Line spacing: single

Page 27: [23] Formatted   Kim, Hyerim   10/3/24 9:38:00 PM

English (US)

Page 27: [24] Formatted   Kim, Hyerim   10/3/24 9:38:00 PM

Font color: Auto

Page 27: [24] Formatted   Kim, Hyerim   10/3/24 9:38:00 PM

Font color: Auto

Page 27: [25] Formatted   Kim, Hyerim   10/3/24 9:38:00 PM

Font: Times New Roman, Font color: Auto

Page 27: [26] Formatted   Kim, Hyerim   10/3/24 9:38:00 PM

Left, Line spacing: single

Page 27: [27] Formatted   Kim, Hyerim   10/3/24 9:38:00 PM

Font: Times New Roman, English (US)

Page 27: [28] Formatted   Kim, Hyerim   10/3/24 9:38:00 PM

Font: Times New Roman, Font color: Auto

Page 27: [28] Formatted   Kim, Hyerim   10/3/24 9:38:00 PM

Font: Times New Roman, Font color: Auto

Page 27: [29] Formatted   Kim, Hyerim   10/3/24 9:38:00 PM

Font: Times New Roman

Page 27: [30] Formatted   Kim, Hyerim   10/3/24 9:38:00 PM

Left, Line spacing: single

Page 27: [31] Formatted   Kim, Hyerim   10/3/24 9:38:00 PM

Font: Times New Roman, English (US)

Page 27: [32] Formatted   Kim, Hyerim   10/3/24 9:38:00 PM

Font: Times New Roman

Page 27: [32] Formatted   Kim, Hyerim   10/3/24 9:38:00 PM

Font: Times New Roman

Page 27: [33] Formatted   Kim, Hyerim   10/3/24 9:38:00 PM

Font: Times New Roman

Page 27: [34] Formatted   Kim, Hyerim   10/3/24 9:38:00 PM

Left, Line spacing: single

Page 27: [35] Formatted Table   Kim, Hyerim   10/3/24 9:38:00 PM

Formatted Table

Page 27: [36] Formatted   Kim, Hyerim   10/3/24 9:38:00 PM

Font: Times New Roman, English (US)

Page 27: [37] Formatted   Kim, Hyerim   10/3/24 9:38:00 PM

Font: Times New Roman

Page 27: [37] Formatted   Kim, Hyerim   10/3/24 9:38:00 PM

Font: Times New Roman

Page 27: [38] Formatted   Kim, Hyerim   10/3/24 9:38:00 PM

Left, Line spacing: single

Page 27: [39] Formatted   Kim, Hyerim   10/3/24 9:38:00 PM

Font: Times New Roman, English (US)

Page 27: [40] Deleted   Kim, Hyerim   10/3/24 9:38:00 PM

Page 27: [41] Formatted   Kim, Hyerim   10/3/24 9:38:00 PM

Font: Times New Roman, English (US)

Page 27: [42] Formatted   Kim, Hyerim   10/3/24 9:38:00 PM

Left, Line spacing: single

Page 27: [43] Formatted   Kim, Hyerim   10/3/24 9:38:00 PM

Font: Times New Roman, English (US)

Page 27: [44] Formatted   Kim, Hyerim   10/3/24 9:38:00 PM

Font: Times New Roman, English (US)

Page 27: [45] Formatted   Kim, Hyerim   10/3/24 9:38:00 PM

Left, Line spacing: single

Page 27: [46] Formatted   Kim, Hyerim   10/3/24 9:38:00 PM

Font: Times New Roman, English (US)

Page 27: [47] Formatted   Kim, Hyerim   10/3/24 9:38:00 PM

Font: Times New Roman, English (US)

Page 27: [48] Deleted   Kim, Hyerim   10/3/24 9:38:00 PM

Page 27: [49] Formatted   Kim, Hyerim   10/3/24 9:38:00 PM

Font: Times New Roman

Page 27: [50] Formatted Table   Kim, Hyerim   10/3/24 9:38:00 PM

Formatted Table

Page 27: [51] Formatted   Kim, Hyerim   10/3/24 9:38:00 PM

Font: Times New Roman, English (US)

Page 27: [52] Formatted   Kim, Hyerim   10/3/24 9:38:00 PM

Font: Times New Roman

Page 27: [52] Formatted   Kim, Hyerim   10/3/24 9:38:00 PM

Font: Times New Roman

Page 27: [53] Formatted   Kim, Hyerim   10/3/24 9:38:00 PM

Font: Times New Roman

Page 27: [54] Formatted   Kim, Hyerim   10/3/24 9:38:00 PM

Left, Line spacing: single

Page 27: [55] Formatted Table   Kim, Hyerim   10/3/24 9:38:00 PM

Formatted Table

Page 27: [56] Formatted   Kim, Hyerim   10/3/24 9:38:00 PM

Font: Times New Roman, English (US)

Page 27: [57] Formatted   Kim, Hyerim   10/3/24 9:38:00 PM

Font: Times New Roman

Page 27: [57] Formatted   Kim, Hyerim   10/3/24 9:38:00 PM

Font: Times New Roman

Page 27: [58] Formatted   Kim, Hyerim   10/3/24 9:38:00 PM

Font: Times New Roman

Page 27: [59] Formatted   Kim, Hyerim   10/3/24 9:38:00 PM

Left, Line spacing: single

Page 27: [60] Formatted   Kim, Hyerim   10/3/24 9:38:00 PM

Font: Times New Roman, English (US)

Page 27: [61] Formatted   Kim, Hyerim   10/3/24 9:38:00 PM

Font: Times New Roman

Page 27: [61] Formatted   Kim, Hyerim   10/3/24 9:38:00 PM

Font: Times New Roman

Page 27: [62] Formatted   Kim, Hyerim   10/3/24 9:38:00 PM

Font: Times New Roman, Font color: Auto, English (UK)

Page 27: [63] Formatted   Kim, Hyerim   10/3/24 9:38:00 PM

Left, Line spacing: single

Page 27: [64] Formatted Table   Kim, Hyerim   10/3/24 9:38:00 PM

Formatted Table

Page 27: [65] Formatted   Kim, Hyerim   10/3/24 9:38:00 PM

Font: Times New Roman, English (US)

Page 27: [66] Formatted   Kim, Hyerim   10/3/24 9:38:00 PM

Font: Times New Roman, Font color: Auto, English (UK)

Page 27: [66] Formatted   Kim, Hyerim   10/3/24 9:38:00 PM

Font: Times New Roman, Font color: Auto, English (UK)

Page 27: [67] Formatted   Kim, Hyerim   10/3/24 9:38:00 PM

Font: Times New Roman

Page 27: [68] Formatted   Kim, Hyerim   10/3/24 9:38:00 PM

Left, Line spacing: single

Page 27: [69] Formatted   Kim, Hyerim   10/3/24 9:38:00 PM

Font: Times New Roman, English (US)

Page 27: [70] Formatted   Kim, Hyerim   10/3/24 9:38:00 PM

Font: Times New Roman

Page 27: [70] Formatted   Kim, Hyerim   10/3/24 9:38:00 PM

Font: Times New Roman

Page 27: [71] Formatted   Kim, Hyerim   10/3/24 9:38:00 PM

Left, Line spacing: single

Page 27: [72] Formatted   Kim, Hyerim   10/3/24 9:38:00 PM

Font: Times New Roman, English (US)

Page 27: [73] Formatted   Kim, Hyerim   10/3/24 9:38:00 PM

Font: Times New Roman, English (US)

Page 27: [74] Deleted   Kim, Hyerim   10/3/24 9:38:00 PM

Page 27: [75] Formatted   Kim, Hyerim   10/3/24 9:38:00 PM

Font: Times New Roman

Page 27: [76] Formatted Table   Kim, Hyerim   10/3/24 9:38:00 PM

Formatted Table

Page 27: [77] Formatted   Kim, Hyerim   10/3/24 9:38:00 PM

Font: Times New Roman, English (US)

Page 27: [78] Formatted   Kim, Hyerim   10/3/24 9:38:00 PM

Font: Times New Roman

Page 27: [78] Formatted   Kim, Hyerim   10/3/24 9:38:00 PM

Font: Times New Roman

Page 27: [79] Deleted   Kim, Hyerim   10/3/24 9:38:00 PM

Page 27: [80] Formatted   Kim, Hyerim   10/3/24 9:38:00 PM

Font: Times New Roman

Page 27: [81] Formatted Table   Kim, Hyerim   10/3/24 9:38:00 PM

Formatted Table

Page 27: [82] Formatted   Kim, Hyerim   10/3/24 9:38:00 PM

Font: Times New Roman, English (US)

Page 27: [83] Formatted   Kim, Hyerim   10/3/24 9:38:00 PM

Font: Times New Roman

Page 27: [83] Formatted   Kim, Hyerim   10/3/24 9:38:00 PM

Font: Times New Roman

Page 27: [84] Deleted   Kim, Hyerim   10/3/24 9:38:00 PM

Page 27: [85] Formatted   Kim, Hyerim   10/3/24 9:38:00 PM

Font: Times New Roman

Page 27: [86] Formatted Table   Kim, Hyerim   10/3/24 9:38:00 PM

Formatted Table

Page 27: [87] Formatted   Kim, Hyerim   10/3/24 9:38:00 PM

Font: Times New Roman, English (US)

Page 27: [88] Formatted   Kim, Hyerim   10/3/24 9:38:00 PM

Font: Times New Roman

Page 27: [88] Formatted   Kim, Hyerim   10/3/24 9:38:00 PM

Font: Times New Roman

Page 27: [89] Formatted   Kim, Hyerim   10/3/24 9:38:00 PM

Font: Times New Roman, Font color: Auto

Page 27: [90] Formatted   Kim, Hyerim   10/3/24 9:38:00 PM

Left, Line spacing: single

Page 27: [91] Formatted   Kim, Hyerim   10/3/24 9:38:00 PM

Font: Times New Roman, English (US)

Page 27: [92] Formatted   Kim, Hyerim   10/3/24 9:38:00 PM

Font: Times New Roman, Font color: Auto

Page 27: [92] Formatted   Kim, Hyerim   10/3/24 9:38:00 PM

Font: Times New Roman, Font color: Auto

Page 27: [93] Deleted   Kim, Hyerim   10/3/24 9:38:00 PM

Page 27: [94] Formatted   Kim, Hyerim   10/3/24 9:38:00 PM

Font: Times New Roman, Font color: Auto

Page 27: [95] Formatted Table   Kim, Hyerim   10/3/24 9:38:00 PM

Formatted Table

Page 27: [96] Formatted   Kim, Hyerim   10/3/24 9:38:00 PM

Font: Times New Roman, English (US)

Page 27: [97] Formatted   Kim, Hyerim   10/3/24 9:38:00 PM

Font: Times New Roman, Font color: Auto

Page 27: [97] Formatted   Kim, Hyerim   10/3/24 9:38:00 PM

Font: Times New Roman, Font color: Auto

Page 27: [98] Deleted   Kim, Hyerim   10/3/24 9:38:00 PM

Page 27: [99] Formatted   Kim, Hyerim   10/3/24 9:38:00 PM

Font: Times New Roman

Page 27: [100] Formatted Table   Kim, Hyerim   10/3/24 9:38:00 PM

Formatted Table

Page 27: [101] Formatted   Kim, Hyerim   10/3/24 9:38:00 PM

Font: Times New Roman, English (US)

Page 27: [102] Formatted   Kim, Hyerim   10/3/24 9:38:00 PM

Font: Times New Roman

Page 27: [102] Formatted   Kim, Hyerim   10/3/24 9:38:00 PM

Font: Times New Roman

Page 27: [103] Formatted   **Kim, Hyerim**   **10/3/24 9:38:00 PM**

Font: Times New Roman

Page 27: [103] Formatted   **Kim, Hyerim**   **10/3/24 9:38:00 PM**

Font: Times New Roman

Page 27: [104] Formatted   **Kim, Hyerim**   **10/3/24 9:38:00 PM**

Font: Times New Roman

Page 27: [104] Formatted   **Kim, Hyerim**   **10/3/24 9:38:00 PM**

Font: Times New Roman

Page 27: [105] Deleted   **Kim, Hyerim**   **10/3/24 9:38:00 PM**

Page 27: [106] Formatted   **Kim, Hyerim**   **10/3/24 9:38:00 PM**

Font: Times New Roman

Page 27: [107] Formatted Table   **Kim, Hyerim**   **10/3/24 9:38:00 PM**

Formatted Table

Page 27: [108] Formatted   **Kim, Hyerim**   **10/3/24 9:38:00 PM**

Font: Times New Roman, English (US)

Page 27: [109] Formatted   **Kim, Hyerim**   **10/3/24 9:38:00 PM**

Font: Times New Roman

Page 27: [109] Formatted   **Kim, Hyerim**   **10/3/24 9:38:00 PM**

Font: Times New Roman

Page 27: [110] Formatted   **Kim, Hyerim**   **10/3/24 9:38:00 PM**

Font: Times New Roman, Font color: Auto, English (UK)

Page 27: [110] Formatted   **Kim, Hyerim**   **10/3/24 9:38:00 PM**

Font: Times New Roman, Font color: Auto, English (UK)

Page 27: [111] Formatted   **Kim, Hyerim**   **10/3/24 9:38:00 PM**

Font: Times New Roman, Font color: Auto, English (UK)

Page 27: [111] Formatted   **Kim, Hyerim**   **10/3/24 9:38:00 PM**

Font: Times New Roman, Font color: Auto, English (UK)

Page 27: [112] Deleted   **Kim, Hyerim**   **10/3/24 9:38:00 PM**

Page 27: [113] Formatted   **Kim, Hyerim**   **10/3/24 9:38:00 PM**

Font: Times New Roman

Page 27: [114] Formatted Table   **Kim, Hyerim**   **10/3/24 9:38:00 PM**

Formatted Table

Page 27: [115] Formatted   **Kim, Hyerim**   **10/3/24 9:38:00 PM**

Font: Times New Roman, English (US)